2015-04-09

Evaluation of the utility of static and adaptive mesh refinement for idealized tropical cyclone problems in a spectral element shallow water model

Evaluation of the utility of static and adaptive mesh refinement for idealized tropical cyclone problems in a spectral element shallow water model

Eric A. Hendricks *

Marine Meteorology Division, Naval Research Laboratory, Monterey, CA, USA

Michal A. Kopera and Francis X. Giraldo

Department of Mathematics, Naval Postgraduate School, Monterey, CA, USA

Melinda S. Peng, James D. Doyle, and Qingfang Jiang

Marine Meteorology Division, Naval Research Laboratory, Monterey, CA, USA

Mon. Wea. Rev

Submitted: April 9, 2015

* *Corresponding author address:* Eric A. Hendricks, Naval Research Laboratory, Monterey, CA 93943

E-mail: eric.hendricks@nrlmry.navy.mil

ABSTRACT

The utility of static and adaptive mesh refinement (SMR and AMR, respectively) are examined for idealized tropical cyclone (TC) simulations in a spectral element f-plane shallow water model. The SMR simulations have varying sizes of the statically refined meshes (geometry-based) while the AMR simulations use a potential vorticity (PV) threshold to adaptively refine the mesh to the evolving TC. Numerical simulations are conducted for four cases: (i) TC-like vortex advecting in a uniform flow, (ii) binary vortex interaction, (iii) barotropic instability of a PV ring, and (iv) barotropic instability of a thin strip of PV. For each case, a high resolution "truth" simulation is compared to two different SMR simulations and three different AMR simulations for accuracy and efficiency. The multiple SMR and AMR simulations have variations in the number of fully-refined elements in the vicinity of the TC. For these idealized cases, it is found that the SMR and AMR simulations are able to resolve the vortex dynamics as well as the "truth" runs, with no significant loss in accuracy in the refined region in the vortex vicinity and with significant speed-ups (factor of 2-5). The overall accuracy is enhanced by a greater area of fully refined mesh in both the SMR and AMR simulations. While these results are highly idealized, they demonstrate the potential for SMR and AMR for the numerical simulation of TCs in three dimensions and more complex models.

1. Introduction

Atmospheric motions span a multitude of different spatial and temporal scales. Examples are planetary waves at spatial scales of 10^6 m which evolve over days to boundary layer turbulent eddies at scales of 10^1 m which evolves over minutes. With current computational resources, it is not possible to simulate the entire spectrum of atmospheric flows. One of the goals in the design of next generation numerical weather prediction (NWP) models is that they be unified, or that one nonhydrostatic dynamical core has the capability of simulating a wide-spectrum atmospheric spatial and temporal scales of motion, from microscale to global, and weather to climate. Severe and high-impact weather can often take the form of localized weather systems, such as severe thunderstorms, tornadoes, fronts, and tropical cyclones. With limited computational resources, it would be ideal to perform local mesh refinement to resolve the details of these features, while resolving the large-scale features (e.g., synoptic scale high pressure systems) at coarser resolution.

Currently, the primary method for tackling this scale discrepancy is by utilizing multiply nested numerical weather prediction (NWP) models (Kurihara et al. 1979; Hodur 1997; Kurihara et al. 1998; Skamarock et al. 2005; Doyle et al. 2014). However, a number of drawbacks exist with this method. First, there exist multiple lateral boundaries, often with the existence of non-physical blending zones. Secondly, there is inefficiency in performing the same forecast on each nest since the nests are embedded within each other. Thirdly, due to the extra communication required between nests, it is not expected that these setups would scale that efficiently on multiple processors. An alternative method to embedded nests is static or adaptive mesh refinement. In the former method, a mesh could be statically refined over a region of interest (e.g., a city or coastline) providing more fine scale details of the flow there. In the latter method, the mesh could adaptively refine and de-refine based on some feature of interest, such as a tropical cyclone (TC). The earlier work of Berger and Oliger (1984) and Skamarock and Klemp (1993) demonstrated the utility of AMR for hyperbolic equations. A review of the current state of AMR for atmospheric modeling is described in Jablonowski (2004) and Behrens (2006).

The purpose of the present study is to examine the utility of both SMR and AMR for ideal TC simulations in a next generation dynamical core. The model is a planar spectral element shallow water model, with similar numerical methods used in the Nonhydrostatic Unified Model of the Atmosphere (NUMA; Giraldo and Restelli 2008). We examine the utility of SMR and AMR for four flows, representing idealizations of TC dynamics in the real atmosphere. First, we examine the a TC advecting in a uniform flow, representing a TC tracking in the atmosphere in steady environmental flow. Secondly, a binary vortex interaction is examined, representing the interaction of two TCs that are close together. Thirdly, instabilities and mixing processes are examined in the hurricane inner-core (eye and eyewall). Fourth, the instability of the intertropical convergence zone (ITCZ), its breakdown, and formation of TC-like vortices. In each case, we compare a series of SMR and AMR simulations with variable regions of refined mesh to a "truth" simulation with uniform refined mesh in order to obtain an understanding of efficiency and accuracy tradeoffs. The remainder of this paper is organized as follows. In section 2, the continuous model equations and numerical method are given. Each experimental setup is given in section 3, along with details of the spatial and temporal discretization. The results from each experiment are given and discussed in section 4. A summary of the main findings are given in section 5.

2. Model equations and numerical method

a. Continuous equations

The model is based upon the divergent barotropic (shallow water) equations in Cartesian coordinates on an f-plane. The governing equations are

$$\frac{\partial u}{\partial t} + u\frac{\partial u}{\partial x} + v\frac{\partial u}{\partial y} - fv + g\frac{\partial h}{\partial x} = 0 \tag{1}$$

$$\frac{\partial v}{\partial t} + u\frac{\partial v}{\partial x} + v\frac{\partial v}{\partial y} + fu + g\frac{\partial h}{\partial y} = 0 \tag{2}$$

$$\frac{\partial h}{\partial t} + \frac{\partial (uh)}{\partial x} + \frac{\partial (vh)}{\partial y} = 0, \tag{3}$$

where u is the zonal momentum per unit mass, v is the meridional momentum per unit mass, h is the fluid depth, and f is the Coriolis parameter. An important property of the unforced, inviscid shallow water equations (1)-(3) is the material conservation of potential vorticity,

$$\frac{DP}{Dt} = 0, \tag{4}$$

where $P = (f + \zeta)/h$ is the potential vorticity, where $\zeta = \partial v/\partial x - \partial u/\partial y$ is the relative vorticity and $D/Dt = (\partial/\partial t) + u(\partial/\partial x) + v(\partial/\partial y)$ is the material derivative.

b. Numerical method and mesh refinement algorithms

The flux form of the continous shallow water equations (1)–(3) are discretized using the continuous Galerkin (CG), or spectral element, numerical method. The flux form shallow water equations are written in compact vector form as follows:

$$\frac{\partial \mathbf{U}}{\partial t} + \nabla \cdot \left(\frac{\mathbf{U} \otimes \mathbf{U}}{\varphi} + \frac{1}{2}\varphi^2 \mathbf{I}_2 \right) + f\mathbf{k} \times \mathbf{U} = 0 \tag{5}$$

$$\frac{\partial \varphi}{\partial t} + \nabla \cdot \mathbf{U} = 0, \tag{6}$$

where $\mathbf{U} = \varphi \mathbf{u}$, $\mathbf{u} = (u, v, 0)^T$ is the velocity vector (where the superscript T denotes the transpose), $\varphi = gh$ with h being the fluid height and g the gravitational constant. Other quantities requiring definition include: $\mathbf{I}_2 \in \mathcal{R}^2$ is an identity matrix, $\mathbf{k} = (0, 0, 1)^T$ is the vector pointing upwards (along the z-coordinate which coincides with the direction along which h is measured), $\otimes$ denotes the tensor product operator, and $\nabla \cdot$ denotes the divergence operator.

High order CG methods for the shallow water equations are given in Ma (1993) and Taylor et al. (1997), and the numerical model used is this study is based upon the specific methods discussed in Giraldo (2001) and Giraldo and Restelli (2008). The spectral element method has been applied to numerous idealized test cases, as well as more complicated idealized tests cases of atmospheric phenomena, such as moist experiments of a squall line (Gabersek et al. 2012).

A brief overview of the elemental CG method is given here. Given a computational domain Ω, the domain is first decomposed into a number of elements N_e as

$$\Omega = \bigcup_{1}^{N_e} \Omega_e \tag{7}$$

where Ω_e is one element. In each element, the weak integral form of the shallow water equations above is taken, and the solution is expanded as

$$q_N(x, y, t) = \sum_{j=1}^{M_N} \chi_j(x, y) q_j(t) \tag{8}$$

where q_N is a prognostic variable, $M_N = (N+1)^2$, N is the polynomial order, and χ_j is a local basis function. In the CG method, neighboring elements share interface points and in each element the solution is obtained at the Legendre-Gauss-Lobatto (LGL) nodal points. As an example, Fig. 1 shows the LGL nodal points inside one element for $N = 5$.

The mesh refinement algorithm is based upon Kopera and Giraldo (2014, 2015), and uses a forest of quad trees (i.e., each internal node has four children), similar to the approach used by St-Cyr et al. (2008). In the refinement procedure, the polynomial order N is held constant, while the mesh is refined (i.e., h-refinement is done instead of p-refinement). For the experiments here, a maximum of two levels of mesh refinement is used, so that a fully refined element is four times the horizontal resolution of a coarse element. Additionally, the refinement algorithm includes the functionality to generate an arbitrary number of layers of refined mesh cells extending away from the feature of interest. This is hereafter referred to as the "buffer" region. The AMR criterion for this study is the potential vorticty P, and refinement and coarsening of the elements is accomplished based on a threshold in P. An attractive feature of PV is that linear inertia-gravity waves have zero PV, eliminating the possibility of AMR tracking fast-mode inertia-gravity waves. The SMR criterion is based subjectively on different area sizes around the feature of interest.

3. Initial conditions and model setup

Four different test cases are examined and described in detail below. These cases are: (i) TC vortex moving in a uniform flow, (ii) binary vortex interaction, (iii) dynamic instability of the hurricane eyewall, eye mesovortex formation and mixing between the eyewall and eye, and (iv) formation of TC-like vortices from the barotropic instability of a shear zone. These cases are idealizations of TC dynamics occurring in the real atmosphere. In order to relate the simulations to the real processes, Fig. 2 shows an example real-case scenario that each test case is designed to represent. In Fig. 2a, Hurricane Andrew is shown moving west towards Florida, being advected by the easterly flow around the subtropical ridge to its north (case 1 idealization). In Fig. 2b, the binary vortex interaction of two storms Typhoons Melor and Parma are shown. The differential advection induced from each cyclone advects the other creating a net cyclonic motion (the Fujiwhara effect; Fujiwhara 1921) (case 2 idealization). In Fig. 2c, the instability and break down of the eyewall of Hurricane Dolly (2008) is shown, leading to an asymmetric radar reflectivity pattern there (case 3 idealization). Finally, in Fig. 2d, the instability and breakdown of the ITCZ is shown over days. The deep convection along the ITCZ is observed to undulate and finally breakdown into distinct tropical cyclones (case 4 idealization).

a. *Case 1: TC vortex advecting in a uniform flow*

The first test case is a TC-like vortex advecting in a uniform flow, which is an idealization of a TC moving with the environmental flow in the atmosphere. The initial vortex is constructed as a Rankine vortex in polar coordinates (r, ϕ, where $r = (x^2 + y^2)^{1/2}$ and ϕ is the azimuthal angle in radians) according to

$$v_\phi(r,\phi,0) = \begin{cases} \zeta_1 r/2 & 0 \le r \le r_1, \\ \zeta_1 r_1^2/(2r) & r_1 \le r < \infty, \end{cases} \tag{9}$$

where v_ϕ is the tangential velocity, $\zeta_1 = 1 \times 10^{-3}$ s^{-1} and $r_1 = 50$ km. With these parameters, the peak tangential velocity at $r = 50$ km is 25 m s^{-1}. A smooth radial decay function

$(1 - r/r_{\mathrm{cut}})^2$ is added to the tangential winds so that $v_\phi(r, \phi, 0) = 0$ at r_{cut}, with a cutoff radius $r_{\mathrm{cut}} = 220$ km. The vortex Cartesian momentum components u and v are next specified and then the uniform zonal flow $u_0 = 10$ m s^{-1} is added to u. This experiment is done on an f-plane with $f = 0$. The initial balanced fluid depth is determined by solving the nonlinear balance equation

$$g\nabla^2 h = f\nabla^2\psi - 2\left[\left(\frac{\partial^2\psi}{\partial x\partial y}\right)^2 - \frac{\partial^2\psi}{\partial x^2}\frac{\partial^2\psi}{\partial y^2}\right], \tag{10}$$

using the CG method, where $\zeta = \nabla^2\psi$, $u = \partial\psi/\partial y$ and $v = -\partial\psi/\partial x$.

The equations are solved on a square domain of 600 km $\times$ 600 km. The setup is a zonal channel flow, with no-flux boundary conditions applied at the north and south lateral boundaries, and periodic boundary conditions applied at the west and east boundaries. The simulation is run for one revolution, so the final TC is located at the starting point, for comparison to the analytic solution which is the initial condition.

b. Case 2: Binary vortex interaction

The second case is a binary vortex interaction (Dritschel and Waugh 1992; Prieto et al. 2001, 2003). In this case, two TC-like vortices are offset by a certain distance and allowed to interact with one another. Depending on the offset distance, and the size and intensity of each vortex, different interactions can occur such as complete merger, complete straining out, partial straining out, elastic interaction (Prieto et al. 2003). The case we choose here is an elastic interaction, where each vortex retains its shape, but the interaction of the two vortices cause a net cyclonic motion (the Fujiwhara effect).

The initial condition for the binary vortex interaction case consists of two offset Rankine vortices. Each vortex is constructed according to

$$v_\phi(r,\phi,0) = \begin{cases} \zeta_1 r/2 & 0 \le r \le r_1, \\ \zeta_1 r_1^2/(2r) & r_1 \le r < \infty, \end{cases} \tag{11}$$

where $\zeta_1 = 1 \times 10^{-3}$ s^{-1}. The first vortex is positioned at $(x, y) = (15, 0)$ km and the second vortex is positioned at $(x, y) = (-15, 0)$ km. The same r_{cut} as in case 1 is applied to each vortex to ensure the winds decay to zero before the lateral boundary. No-flux boundary conditions are used at each lateral boundary. The nonlinear balance equation (8) is solved using the initial condition of both vortices in order to obtain the corresponding $h(x, y, 0)$ field, only with $f = 1.0 \times 10^{-4}$ s^{-1}.

c. Case 3: Barotropic instability of the hurricane eyewall

The third case is the barotropic instability of the hurricane eyewall. The hurricane eyewall can largely be described as a three-region model: (i) low vorticity eye, (ii) high vorticity eyewall, and (iii) low vorticity environment. Observations of such vorticity structures in real hurricanes are given in Kossin and Eastin (2001) and Hendricks et al. (2012). An idealization of this structure can be constructed according to Schubert et al. (1999) using the tangential velocity profile

$$v_\phi(r,\phi,0) = \frac{1}{2r} \begin{cases} \xi_1 r^2 + \xi_2 r^2 & 0 \le r \le r_1 \\ \xi_1 r_1^2 + \xi_2 r_2^2 & r_1 \le r \le r_2, \\ \xi_1 r_1^2 + \xi_2 r_2^2 & r_2 \le r \le \infty \end{cases} \tag{12}$$

which defines a discrete three region model of axisymmetric relative vorticity

$$\zeta(r,\phi,0) = \frac{1}{r}\frac{\partial(rv)}{\partial r} = \begin{cases} \xi_1+\xi_2 & 0 \le r \le r_1 \\ \xi_2 & r_1 \le r \le r_2, \\ 0 & r_2 \le r \le \infty \end{cases} \tag{13}$$

Here $\xi_1 = -3 \times 10^{-3}$ s^{-1}, $\xi_2 = 3 \times 10^{-3}$ s^{-1}, $r_1 = 40$ km and $r_2 = 50$ km. The hurricane eye is defined as the region less than r_1, the eyewall is defined as the region between r_1 and r_2, and the environment is defined as the region between r_2 and infinity. Similar to the previous experiments, a smooth radial decay function $(1 - r/r_{\mathrm{cut}})^2$ is added to the tangential winds so that $v_\phi(r,\phi,0) = 0$ at r_{cut}. The cutoff radius $r_{\mathrm{cut}} = 220$ km. No-flux boundary conditions are used at each lateral boundary.

The nature of the instability is as follows. Each vorticity gradient of the ring supports a vortex Rossby wave (Montgomery and Kallenbach 1997). The inner vortex Rossby wave progrades relative the mean flow, while the outer vortex Rossby wave retrogrades relative to the mean flow. Thus it is possible for each of these waves to have the same angular velocity, or be phase-locked, leading to the barotropic instability of the ring. A comprehensive linear stability analysis of this structure is provided by Schubert et al. (1999), and nonlinear simulations and discussions of aspects of this problem are given in Kossin and Schubert (2001) and Hendricks et al. (2009).

To initiate the instability process, a broadband perturbation was added to the basic state vorticity (13) of the form

$$\zeta'(r,\phi,0) = \zeta_{amp} \sum_{m=1}^{8} \cos(m\phi + \phi_m) \quad \times \begin{cases} 0 & 0 \le r \le r_1, \\ 1 & r_1 \le r \le r_2, \\ 0 & r_2 \le r < \infty, \end{cases} \tag{14}$$

where $\zeta_{\rm amp} = 1.0 \times 10^{-5}$ s^{-1} is the amplitude and ϕ_m the phase of azimuthal wavenumber m. For this set of experiments, the phase angles ϕ_m were chosen to be random numbers in the range $0 \le \phi_m \le 2\pi$. In real hurricanes, the impulse is expected to develop from a wide spectrum of background turbulent and convective motions. Similar to case 1, the nonlinear balance equation (8) is solved to obtain the corresponding $h(x, y, 0)$ field, with $f = 1.0 \times 10^{-4}$ s^{-1}. This ring has a thickness parameter $\delta = r_1/r_2 = 0.8$ and hollowness parameter $\gamma = (\xi_1 + \xi_2)/\zeta_{\rm av} = 0$ (where $\zeta_{\rm av}$ is the average inner-core vorcity). According to the linear stability analysis of Schubert et al. (1999), this ring is most unstable to azimuthal wavenumber $m = 5$, with an e-folding time of 0.57 h.

d. Case 4: Barotropic instability of a shear zone

The fourth test is the examination of the formation of TC-like vortices through the barotropic instability of a region of large horizontal velocity shear. An example of such a process occurring in the real atmosphere is the instability of the inter-tropical convergence zone (ITCZ) in the eastern North Pacific ocean basin, causing it to undulate over days, and eventually break down and form pools of high PV (Fig. 2d). Provided favorable conditions, these PV pools can then form into TCs. An observational and modeling study of the genesis of TCs from this formation mechanism is given in Ferreira and Schubert (1997).

A similar experiment is conducted here. The initial condition is constructed as an idealization of the ITCZ, with easterly flow to the north and westerly flow to the south. A linear function is assumed to bridge the two regions, forming a thin strip of cyclonic vorticity. Mathematically, the initial condition is

$$u(x,y,0) = \begin{cases} -u_0 & y \geq y_0, \\ -u_0 y/y_0 & -y_0 \leq y \leq y_0, \\ u_0 & y \leq -y_0, \end{cases} \tag{15}$$

where $u_0 = 20$ m s^{-1} and $y_0 = 100$ km. Here, $v(x,y,0) = 0$ and h is determined by solving the geostrophic balance equation analytically,

$$h(x,y,0) = \begin{cases} fu_0 y/g & y \geq y_0, \\ [fu_0/(2gy_0)](y^2 + y_0^2) & -y_0 \leq y \leq y_0, \\ -fu_0 y/g & y \leq -y_0, \end{cases} \tag{16}$$

where $f = 1.0 \times 10^{-4}$ s^{-1}.

The strip of PV supports the existence of two counter-propapagating Rossby waves, one on the northern PV gradient which propagates to the east and one on the southern PV gradient which propagates to the west. These two waves can phase-lock and grow, leading to the break down of the strip into vortices. A linear stability analysis of this structure is given by Gill (1980), and here we provide a basic overview of the stability characteristics. Assuming separation of the meriodinal and zonal structure, Rossby wave solutions of the form $\psi'(x,y,t) = \Psi(y)\exp(ik(x-ct))$ are sought, where ψ' is the wave streamfunction. Here, $c = c_r + ic_i$ is the complex phase velocity, and k is the zonal wavenumber. The linear stability analysis of this simple shear zone indicates the most unstable zonal wavenumber $k = 0.3984/y_0 = 3.984 \times 10^{-6}$ m^{-1}, or approximately 1577 km. The domain used here is 8000 km $\times$ 8000 km, therefore the most unstable mode is zonal wavenumber-5. The growth rate $kc_i = 0.2012u_0/y_0 = 4.024 \times 10^{-5}$ s^{-1}, corresponding to an e-folding time of 6.9 hours. In order to initiate the instability, a weak amplitude zonal wavenumber-5 perturbation in vorticity is applied to the region of constant background vorticity (shear zone). The lateral boundary conditions for this run are the same as case 1, no-flux conditions are applied at the north and south boundaries and periodic conditions are applied at the west and east boundaries.

e. *Discretization and model setup*

For all simulations, 5th order polynomials ($N = 5$) are used in each element, and a fourth order explicit Runge-Kutta scheme is used for the temporal integration. No diffusion is used in the experiments, however a modal filter is applied to help control nonlinear instability. For each initial condition listed above, six numerical simulations are performed: (i) a high resolution "truth" simulation (FINE), (ii) A large statically refined mesh around the TC processes (SMR2), (iii) a smaller statically refined mesh (SMR1), (iv) adaptive mesh refinement with a buffer of 6 fully refined elements (AMR3), (v) adaptive mesh refinement with a buffer of 3 fully refined elements (AMR2), and (vi) adaptive meshfinement with no buffer (AMR1). The FINE numerical simulation is the "truth", and is expected to simulate the phenonema with the most accuracy. The varying SMR and AMR simulations are intended to help retain the accuracy of the solution in the vicinity of the TC while also saving on computational time. All simulations are run at the time step of the FINE simulation since our goal is understanding computational aspects only with regard to the spatial variation. The discretization, horizontal resolution, and model setup parameters for all experiments are given in Table 1. Since $N = 5$ polynomials are used in each element, an approximate effective resolution can obtained by dividing the element size by a factor of 5. However, the actual minimum grid spacing is less than this number since the LGL points are unequally spaced, and closer together near the element boundary (Fig. 1).

4. Results

In this section, the qualitative results of each simulation are described, followed by a quantitative analysis of the solution accuracy and computational aspects. For cases 1 and 2 which simulate vortex advection, the results are described in terms of the prognostic variables of zonal and meriodional velocity. For cases 3 and 4 which simulate barotropic instability, the results are described in terms of the PV in order to better illustrate the salient dynamics.

a. Case 1

The initial condition of case 1 is given in Fig. 3. Here the magnitude of the perturbation velocity vector $((u - u_0)^2 + v^2)^{1/2}$ for each simulation is shown in colored contours, with the elements overlayed. Note that only the element boundaries are overlayed, and not the actual grid of nodal points inside each element. The uniform resolution mesh (FINE simulation) is shown in Fig. 3a. In Fig. 3b, the SMR2 simulation is shown which has fully refined mesh for -200 km < y < 200 km. The SMR1 initial condition is shown in Fig. 3c, which has fully refined mesh for -100 km < y < 100 km. The initial conditions for the AMR3, AMR2, and AMR1 simulations are shown in Fig. 1d,e,f, respectively. Here initial condition is adapting to the PV threshold providing fully-refined mesh around the hurricane eyewall (yellow region of stronger winds) and eye. The AMR3, AMR2, and AMR1 buffers are readily evident as refined mesh extending from the center.

In Fig. 4, the simulation results are shown after a half-revolution. At this time, each vortex has moved a distance of 300 km to the right, and the mid-point of each vortex is at the left and right lateral boundaries. The vortex core is well resolved in each simulation and there are no apparent phase errors as the vortex center of each simulation is exactly at the lateral boundary. The outer wind field also appears well resolved by the SMR2, SMR1, AMR3, and AMR2 simulations. There exists some azimuthal variability in the outer wind field in the AMR1 simulation. This could be from some stronger gravity wave activity due to imbalances generated as a result of the coarser representation of the outer wind field. Finally, moving to Fig. 5, each simulation is shown at the final time after one complete revolution, so that the vortex is at its initial position. At this time, all simulations appear to resolve the vortex core well, and there are again no apparent numerical advection errors (moving too slow or fast). Again, here the AMR1 simulation has the most noticable differences in the outer wind field. Overall, qualitatively the results show that all AMR/SMR simulations are able to resolve the core of the TC as it advects in the uniform flow.

b. *Case 2*

The initial condition for the binary vortex interaction is given in Fig. 6. The two Rankine vortices are evident as the two wind maximas. All simulations are able to resolve the vortex core well. Here the SMR2 simulation has statically refined mesh between -200 km < (x,y) < 200 km, and SMR1 simulation has statically refined mesh between -100 km < (x,y) < 100 km. Moving to Fig. 7, each vortex is shown at $t = 12$ h. The vortices have rotated in cyclonic motion approximately 135 degrees and the outer winds of each vortex has advected the other. At this time each simulation has a similar orientation of the binary vortices, indicating that even the AMR1 simulation is rotating the vortices at the correct angular velocity. In Fig. 8, the solution is shown at $t = 24$ h, after another net cyclonic rotation of 135 degrees. At this time, all vortices appear to have a similar orientation with the exception of the AMR1 simulation, which has not rotated cyclonically in the proper amount due to the slight weakening of the vortex winds. However, all simulations do a reasonable job at capturing the vortex core wind velocity magnitude.

c. *Case 3*

The initial condition of case 3 is given in Fig. 9. Here, a vortex with a very sharp gradient in tangential velocity is shown (ring of elevated PV). The initial condition of each simulation has fully-refined mesh over the ring of elevated PV. The AMR1 simulation (with no buffer) has a couple of coarse mesh cells at the very center as the initial mesh is adapting to the ring of large PV only. In Fig. 10, the simulation is shown at $t = 2.5$ h, as the most unstable mode of hybrid azimuthal wavenumbers $m = 5/6$ is occuring in each simulation. In Fig. 11, the simulation is shown at $t = 5$ h, after the vortex has broken down into mesovortices (evident by separate PV anomalies). Each simulation appears to be resolving these localized features well. In Fig. 12, the simulation is shown as the mesovortices become strained and filamented, and begin to merge into one central monopole. At this time, the structure of the merging vortices looks quite similar in each run, demonstrating that the static and adpative mesh refinement in the local region is working properly. Finally, in Fig. 13, the simulations are shown at $t = 48$ h, after the initial PV ring has mixed into a monopole. All simulations qualitatively have similar structures. The AMR1 simulation has a slightly different orientation of the central monopole.

d. Case 4

The initial condition for case 4 is given for each simulation in Fig. 14. Decreasing amounts of refined mesh are evident in moving from the FINE to the AMR1 case, with the AMR1 case only have refined mesh over the PV strip itself. In Fig. 15, each simulation is shown at $t = 45$ h. Each simulation produces the theoretically predicted most unstable mode of wavenumber-5. Upshear tilt of each PV anomaly associated with the northern and southern counter-propagating Rossby waves is evident. The simulations are shown at $t = 180$ h in Fig. 16. Here the breakdown of the PV strip has resulted in the five separate vortices. All simulations are able to reproduce the five vortices.

e. Error Norms

In order to quantify aspects of these results, normalized L2 errors were computed between the final state in the FINE, or "truth", simulation, and the final state in the SMR/AMR simulations. In order to compute the L2 error norms, the solution at the AMR/SMR meshes at the final time are adapted to the FINE mesh. The normalized L_2 error is defined as

$$L2 = \left(\frac{\sum_{k=1}^{N} (q^{\text{num}}(x_k) - q^{\text{ref}}(x_k))^2}{\sum_{k=1}^{N} q^{\text{ref}}(x_k)^2} \right)^{1/2} \tag{17}$$

where q is the predicted variable, N is the total number of points, the superscript "num" denotes the numerical simulations, and the superscript "ref" denotes the reference solution (or in this case the FINE solution). The normalized L2 error is computed for the magnitude of the velocity vector $|\mathbf{U} = (u, v)|$ and the geopotential $\varphi = gh$. Since we are interested in how well the SMR/AMR simulations resolve the local TC processes in comparison to the FINE simulations, the L2 errors are computed in two regions: (i) the entire domain, and (ii) in the localized region in which the AMR/SMR simulations are designed to resolve. For (ii), this region was defined as $r < 100$ km for cases 1, 2, and 3, and $|y| < 500$ km for case 4. These correspond to the regions of large PV in each case.

The L2 error norms for (i) and (ii) are shown in Figs. 17 and 18, respectively. In both figures, the green bars are the L2 errors in the magnitude of the velocity vector and the black bars are the L2 errors in the magnitude of fluid depth. In Fig. 17, for each case, there is a general trend of decreasing L2 error norms moving from the AMR to the SMR to the FINE simulations. In Fig. 17a, in terms of the velocity vector magnitude, the AMR1 simulation has one order of magnitude larger error than the AMR2, AMR3, and SMR1 simulations (10^{-2}

versus 10^{-3}). The SMR2 simulation has the lowest errors (10^{-4}). A similar trend is evident for φ, however the AMR1 simulation has a significantly larger error than the other runs. In Fig. 17b, the results are shown for case 2. A similar trend is evident, however in this case the AMR1 simulation L2 error in φ is not as significant. In Fig. 17c, a similar result is also seen in the instability case. Moving to Fig. 17d, the results are broadly consistent with the previous panels, however in this case the L2 error in φ shows a continuing decrease, rather than asymptoting as in the previous results. Overall, the results for the entire domain indicate that the SMR2 simulations are most accurate. There are not significant differences between the AMR2, AMR3, and SMR1 simulations. In general, the AMR1 simulation typically has larger errors than the other simulations. In Fig. 18, the same L2 error norms are shown in the region of high PV. Broadly, the results are consistent with Fig. 17, however the errors are generally lower. This is expected since the localized regions have only fully-refined elements. In summary, these results indicate that very high accuracy may be obtained for these TC simulations by using a large statically refined mesh (SMR2). However, the AMR simulations with only three buffer elements (AMR2) are able to produce similar accuracy of the 6 element buffer simulation (AMR3) and statically refined mesh (SMR1) simulations. This is important, since as we will show in the next section, the computational expense of AMR2 is significantly less than AMR3 and SMR1.

f. Computational aspects

Each simulation was executed on a single central processing unit (CPU). In Fig. 19, some computational aspects of the simulations are given. The point ratio is shown in Fig. 19a, and in Fig. 19b, the speedup is given. The point ratio is defined as the inverse of the total number of points of the FINE simulation divided by the average number of points of the AMR simulations (since the points change in time), and the total fixed number of points in the SMR simulations. The speedup is defined as the CPU time of the FINE simulation divided by the CPU time of each of the other simulations. In Fig. 19a, for cases 1–3, the AMR1 simulation has approximately 9–12 times fewer nodal points than the FINE simulation. The AMR1 simulation of case 4 has approximately 5 times fewer points due to the different structure of this atmospheric phenomenon (zonal strip instead of a central vortex). There is approximately a linearly decreasing trend of the point ratio moving to the AMR2, AMR3, SMR1, and SMR2 simulations. Fig. 19b shows the speedup for each simulation over the FINE run. The AMR1 simulation has the largest speedup (factor of 3.5–5), there is a linearly decreasing trend of speedup moving to the FINE simulation. Overall, the speedup is approximately one-half of the point ratio. Since the time step of each simulation is identical, if there were no overhead in refining and de-refining elements, one would expect the speedup factor to be similar to the point ratio. However, this overhead leads to lesser speedups.

g. TC vortex moving through a variable mesh

It has been discussed that in next generation NWP models without AMR, a useful domain structure for simulation of TCs would consist of a large region of refined mesh over the entire tropics, with coarser mesh away from the tropics. In this scenario, while often the TC would remain in the tropics, re-curving TCs would move from the fully-refined mesh to the coarser mesh. It is important to understand how a TC may change in structure moving through such an abrupt mesh boundary. One would expect that without any forcing, the maximum wind speed in the eyewall would be reduced by moving from finely resolved mesh to a coarser mesh, as the eyewall region is less well resolved. The results of this test are given in Fig. 20. Here, the TC vortex is initially centered on a 200 km square box of fully-refined mesh, and then advected to the right in uniform zonal flow (as in case 1). At $t = 4.165$ h, half the eyewall is in the coarse mesh, while half is in the fully-refined mesh. As expected, a slight reduction in the tangential velocity is evident. As the vortex advects into the coarser mesh, then back into the fine mesh, it loses kinetic energy. The fraction of final integrated kinetic energy to initial integrated kinetic energy within $r < 100$ km is 0.999939, indicating that the loss is quite small. These results indicate that the high order methods used here can even broadly preserve aspects of the vortex inner-core structure while moving through an abrupt mesh boundary when the elements are quadrupled in size. This result is broadly consistent with Zarzycki et al. (2014), who found little numerical distortion when a dry TC vortex moved through an abrupt transition of a variable mesh using the spectral element dynamical core of the Community Atmosphere Model (CAM-SE). More energy loss would be expected if a lower polynomial order ($N < 5$) or larger elements were used.

5. Conclusions

A planar shallow water model based on the continuous Galerkin (spectral element) numerical method has been used to examine idealized tropical cyclone (TC) problems, with a focus on the applicability of static and adaptive mesh refinement (SMR and AMR, respectively). Four different idealizations of TC cases in the real atmosphere were simulated in this model, with varying degrees of SMR and AMR. The SMR/AMR simulations were compared to a high resolution "truth" simulation (noted previously as the FINE run) with regard to solution accuracy and computational time. Three different AMR simulations were conducted with varying levels of buffer regions (or the number of extra layers of fine elements added to the finely resolved region). Two different SMR simulations were executed with varying levels of refined mesh. For AMR simulations, a potential vorticity threshold was used for refining and de-refining elements. With regard to solution accuracy, the SMR2 simulation (with the largest area of fully refined mesh) was shown to be superior to the other simulations (at least an order of magnitude lower L2 error) in comparison to the "truth" run. However, the AMR simulations with only 3 buffer elements (AMR2) are shown to be as accurate overall as the AMR simulations with 6 buffer elements (AMR3) and the smaller statically refined mesh simulation SMR1. The AMR simulation with no buffer elements (AMR1) was generally shown to be significantly less accurate than the others. Significant speed-ups were obtained by using AMR. The AMR2 simulations (which are nearly as accurate as the AMR3 and SMR1 simulations) had speed-ups of 2.5–4.5 over the FINE simulation. Thus, these results indicate that AMR can be used at significantly less computational expense to resolve the TC feature as well as the "truth" run, provided a sufficient buffer region exists.

In summary, we wish to note that we have examined static and adaptive mesh refinement for TC applications in a very idealized framework of a shallow water fluid in constant rotation. In the real atmosphere, TCs are three-dimensional phenomena, with complex physics interactions (microphysics, boundary layer, vertical mixing, and radiation), as well as interactions with the environment (such as vertical wind shear and ocean surface fluxes). One of the major challenges in the future with AMR is the development of scale-aware physical parameterizations that will seamlessly represent physical processes across scales. However, these results demonstrate that from a purely dry dynamical modeling standpoint, AMR shows great promise for TC applications.

Acknowledgments.

We gratefully acknowledge support from the Chief of Naval Research PE-0601153N. The codes used in this paper were developed by MAK and FXG during the 4-month long program on Multiscale Numerics in the Atmosphere and Ocean at the Newton Institute, Cambridge University. MAK and FXG gratefully acknowledge the support of the Office of Naval Research through program element PE-0602435N, the National Science Foundation (Division of Mathematical Sciences) through program element 121670, and the Air Force Office of Scientific Research through the Computational Mathematics program. We thank Sasa Gabersek, Alex Reinecke and Kevin Viner for helpful comments.

REFERENCES

Behrens, J., 2006: Adaptive atmospheric modeling: key techniques in grid generation, data structures, and numerical operations with applications. Springer, 2006.

Berger, M. J. and J. Oliger, 1984: Adaptive mesh refinement for hyperbolic partial differential equations. *J. Comput. Phys.*, **53**, 484–512.

Doyle, J. D., R. Hodur, S. Chen, Y. J. amd J.R. Moskaitis, S. Wang, E. A. Hendricks, H. Jin, and T. Smith, 2014: Tropical cyclone prediction using COAMPS-TC. *The Oceanography Soc.*, **27**, 104–115.

Dritschel, D. D. and D. W. Waugh, 1992: Quantification of the inelastic interaction of unequal vortices in two-dimensional vortex dynamics. *Phys. Fluids*, **4**, 1737–1744.

Ferreira, R. N. and W. H. Schubert, 1997: Barotropic aspects of ITCZ breakdown. *J. Atmos. Sci.*, **54**, 261–285.

Fujiwhara, S., 1921: The natural tendency towards symmetry of motion and its application as a principle in meteorology. *Quart. J. Roy. Meteor. Soc.*, **47**, 287–293.

Gabersek, S., F. X. Giraldo, and J. D. Doyle, 2012: Dry and moist idealized experiments with a two-dimensional spectral element model. *Mon. Wea. Rev.*, **140**, 3163–3182.

Gill, A. E., 1980: Some simple solutions for heat-induced tropical circulation. *Quart. J. Roy. Meteor. Soc.*, **106**, 447–462.

Giraldo, F. X., 2001: A spectral element shallow water model on spherical geodesic grids. *Int. J. Numer. Methods Fluids*, **35**, 869–901.

Giraldo, F. X. and M. Restelli, 2008: A study of spectral element and discontinuous Galerkin methods for the Navier–Stokes equations in nonhydrostatic mesoscale atmospheric modeling: Equation sets and test cases. *J. Comput. Phys.*, **227**, 3849–3877.

Hendricks, E. A., B. D. McNoldy, and W. H. Schubert, 2012: Observed inner-core structural variability in Hurricane Dolly (2008). *Mon. Wea. Rev.*, **140**, 4066–4077.

Hendricks, E. A., W. H. Schubert, R. K. Taft, H. Wang, and J. P. Kossin, 2009: Lifecycles of hurricane-like vorticity rings. *J. Atmos. Sci.*, **66**, 705–722.

Hodur, R. M., 1997: The Naval Research Laboratory's Coupled Ocean/Atmosphere Mesoscale Prediction System (COAMPS). *Mon. Wea. Rev.*, **125**, 1414–1430.

Jablonowski, C., 2004: Adaptive grids in weather and climate modeling. Ph.D. Thesis, The University of Michigan (2004).

Kopera, M. A. and F. X. Giraldo, 2014: Analysis of adaptive mesh refinement for IMEX discontinuous Galerkin solutions of the compressible euler equations with application to atmospheric simulations. *J. Comput. Phys.*, **275**, 92–117.

Kopera, M. A. and F. X. Giraldo, 2015: Mass conservation of the unified continuous and discontinuous element-based Galerkin methods on dynamically adaptive grids with application to atmospheric simulations. *J. Comput. Phys.*, in press.

Kossin, J. P. and M. D. Eastin, 2001: Two distinct regimes in the kinematic and thermodynamic structure of the hurricane eye and eyewall. *J. Atmos. Sci.*, **58**, 1079–1090.

Kossin, J. P. and W. H. Schubert, 2001: Mesovortices, polygonal flow patterns, and rapid pressure falls in hurricane-like vortices. *J. Atmos. Sci.*, **58**, 2196–2209.

Kurihara, Y. M., G. J. Tripoli, and M. A. Bender, 1979: Design of a movable nested-mesh primitive equation model. *Mon. Wea. Rev.*, **107**, 239–249.

Kurihara, Y. M., R. E. Tuleya, and M. A. Bender, 1998: The GFDL Hurricane Prediction System and its performance in the 1995 hurricane season. *Mon. Wea. Rev.*, **126**, 1306–1322.

Ma, H., 1993: A spectral element basin model for the shallow water equations. *J. Comput. Phys.*, **109**, 133–149.

Montgomery, M. T. and R. J. Kallenbach, 1997: A theory for vortex Rossby waves and its application to spiral bands and intensity changes in hurricanes. *Quart. J. Roy. Meteor. Soc.*, **123**, 435–465.

Prieto, R., J. P. Kossin, and W. H. Schubert, 2001: Symmetrization of lopsided vorticity monopoles and offset hurricane eyes. *Quart. J. Roy. Meteor. Soc.*, **127**, 1–17.

Prieto, R., B. D. McNoldy, S. R. Fulton, and W. H. Schubert, 2003: A classification of binary tropical cyclone-like vortex interactions. *Mon. Wea. Rev.*, **131**, 2656–2666.

Schubert, W. H., M. T. Montgomery, R. K. Taft, T. A. Guinn, S. R. Fulton, J. P. Kossin, and J. P. Edwards, 1999: Polygonal eyewalls, asymmetric eye contraction, and potential vorticity mixing in hurricanes. *J. Atmos. Sci.*, **56**, 1197–1223.

Skamarock, W. C. and J. B. Klemp, 1993: Adaptive grid refinement for two-dimensional and three-dimensional nonhydrostatic atmospheric flow. *Mon. Wea. Rev.*, **121**, 788–804.

Skamarock, W. C., J. B. Klemp, J. Dudhia, D. O. Gall, D. M. Barker, W. Wang, and J. G. Powers, 2005: A description of the Advanced Research WRF Version 2. Tech. rep., NCAR Tech. Note NCAR/TN-468+STR, 20 pp., Boulder, CO. [Available online at http://www.mmm.ucar.edu/wrf/users/docs/arw_v2.pdf].

St-Cyr, A., C. Jablonowski, J. M. Dennis, H. M. Tufo, and S. J. Thomas, 2008: A comparison of two shallow-water models with nonconforming adaptive grids. *Mon. Wea. Rev.*, **136**, 1898–1922.

Taylor, M., J. Tribbia, and M. Iskandarani, 1997: The spectral element method for the shallow water equations on the sphere. *J. Comput. Phys.*, **130**, 92–108.

Zarzycki, C., C. Jablonowski, and M. Taylor, 2014: Using variable-resolution meshes to model tropical cyclones in Community Atmosphere Model. *Mon. Wea. Rev.*, **142**, 1221–1239.

List of Tables

Table 1. Experiment Parameters

	Case 1	**Case 2**	**Case 3**	**Case 4**
Domain size (km)	600 × 600	600 × 600	600 × 600	8000 × 8000
Fully Refined				
Number of Elements Element spacing (km) Effective resolution (km)	60 × 60 10 2	60 × 60 10 2	60 × 60 10 2	60 × 60 133.33 26.2
Fully Unrefined				
Number of Elements Element spacing (km) Effective resolution (km)	15 × 15 40 8	15 × 15 40 8	15 × 15 40 8	15 × 15 533.33 106.67
Polynomial order	5	5	5	5
Model time step (s)	3	3	3	18

List of Figures

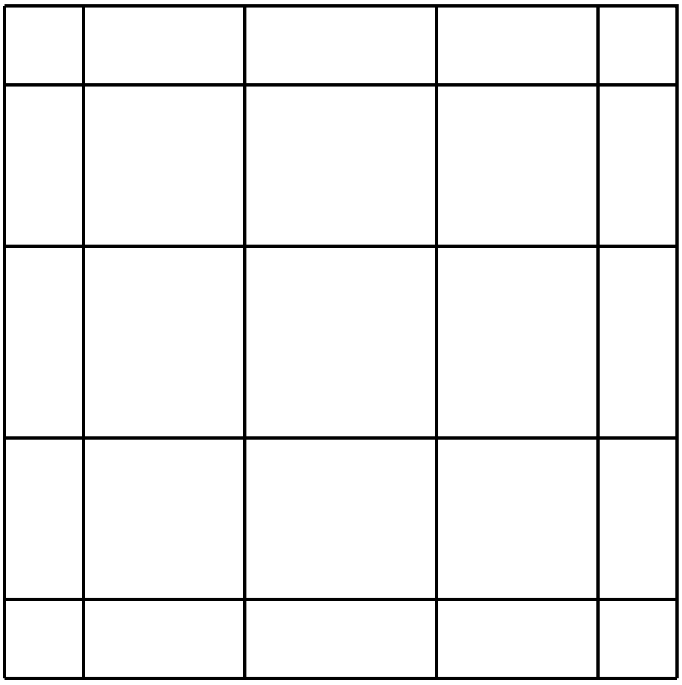

FIG. 1. Grid of Legendre-Gauss-Lobatto nodal points inside one element using $N = 5$ order polynomials as basis functions.

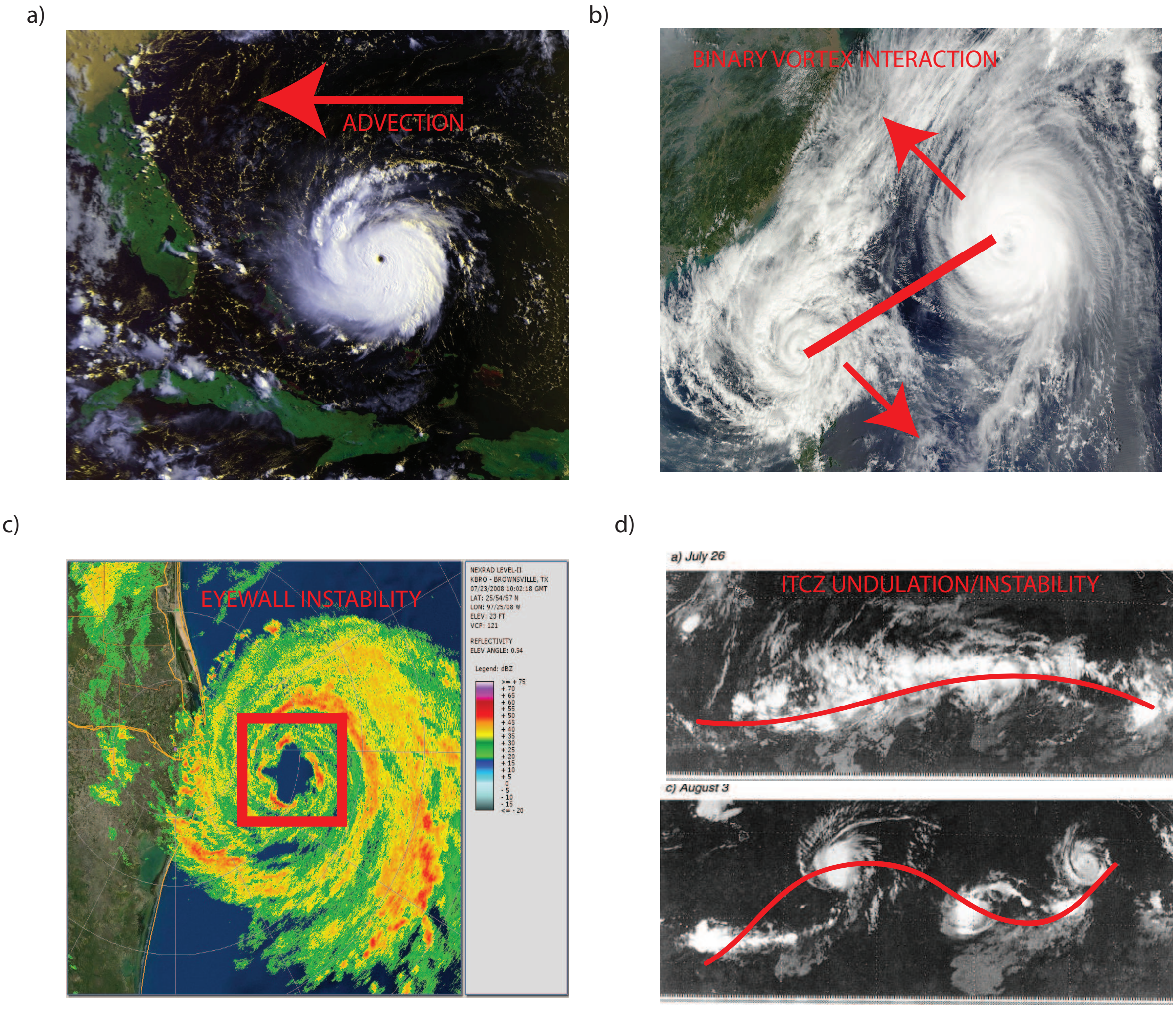

FIG. 2. Satellite and radar observations depicting real TC processes that are being simulated in the idealized framework. Processes are highlighed in bold red. Panels: a) NOAA-12 visible satellite imagery of Hurricane Andrew advecting to the west toward Florida at 1231Z on 23 Aug 1992 (courtesy NOAA), b) MODIS visible satellite imagery of the binary vortex interaction of Tropical Storm Parma and Typhoon Melor on 6 Oct 2009 (courtesy NASA/GSFC), c) Radar image of Hurricane Dolly (2008) at 1002Z 7 Jul 2008 approaching the Texas coast (courtesy NOAA/NWS/KRBO). Significant azimuthal variability in the radar reflectivity in the eyewall is evident, and d) instability and breakdown of the ITCZ into multiple TCs over the timescale of days (reproduced from Ferreira and Schubert (1997)).

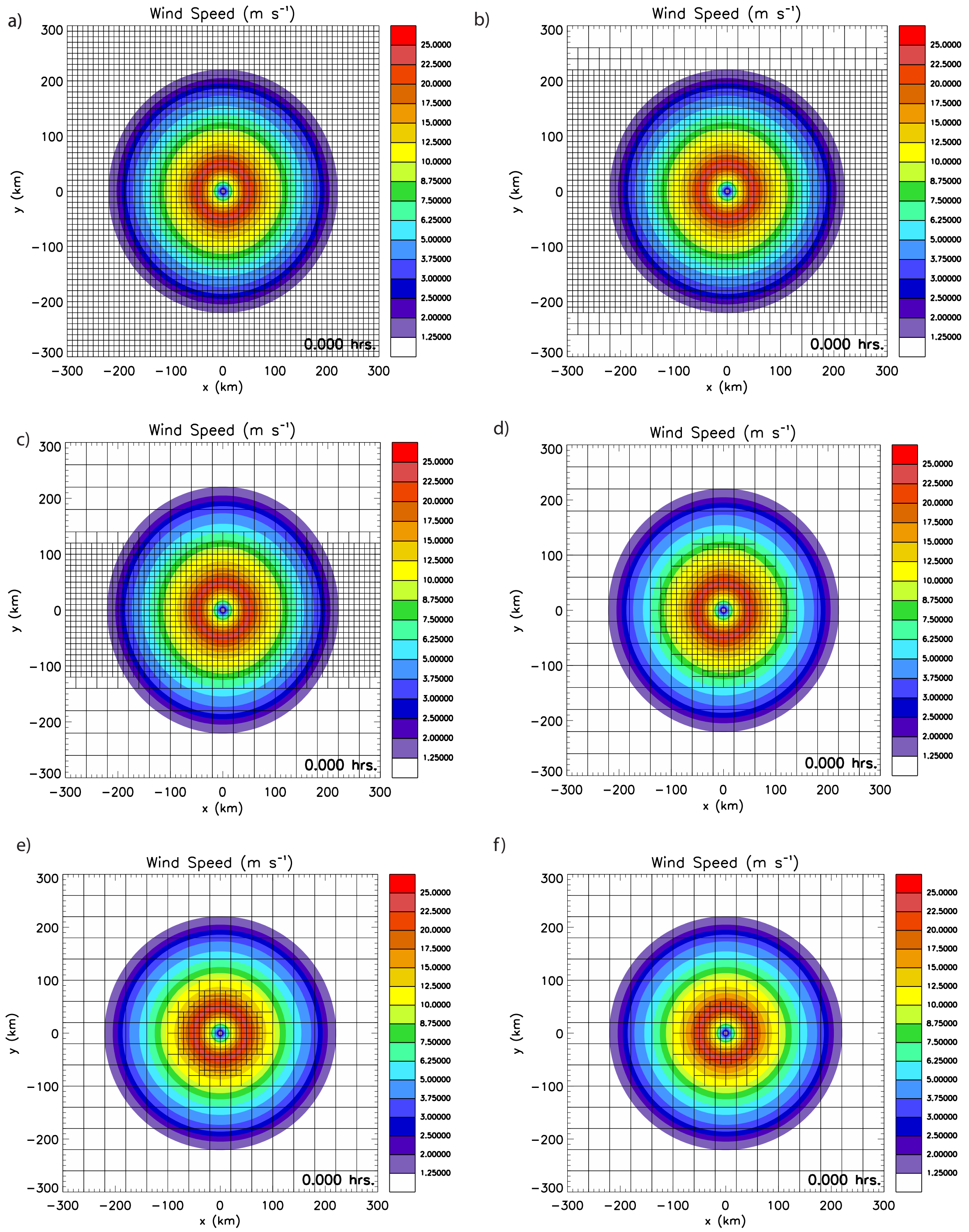

FIG. 3. Initial condition for case 1: advecting vortex. Panels: a) FINE, b) SMR2, c) SMR1, d) AMR3, e) AMR2, f) AMR1.

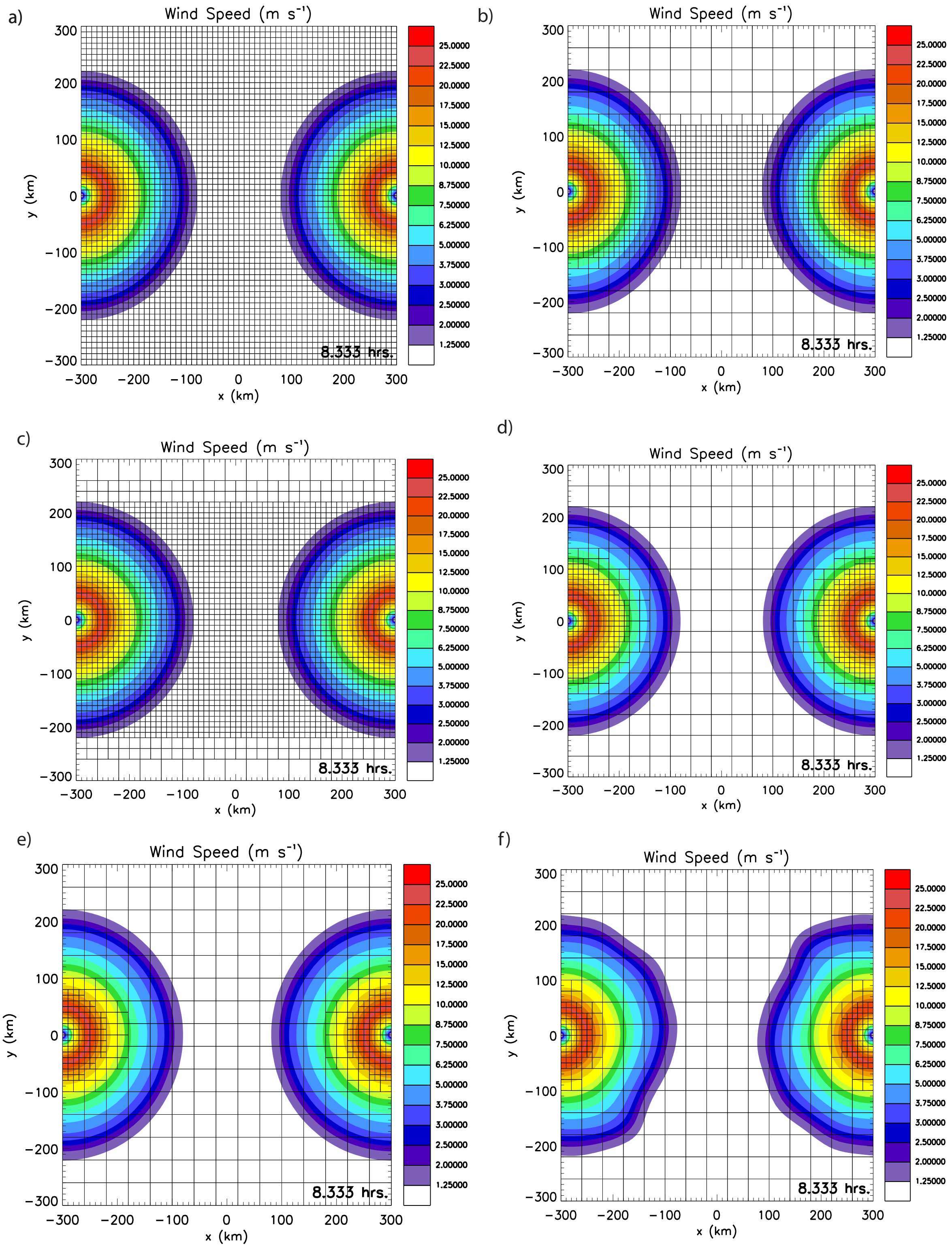

FIG. 4. Simulations of case 1 after one-half revolution, at $t = 8.33$ h. Panels: a) FINE, b) SMR2, c) SMR1, d) AMR3, e) AMR2, f) AMR1.

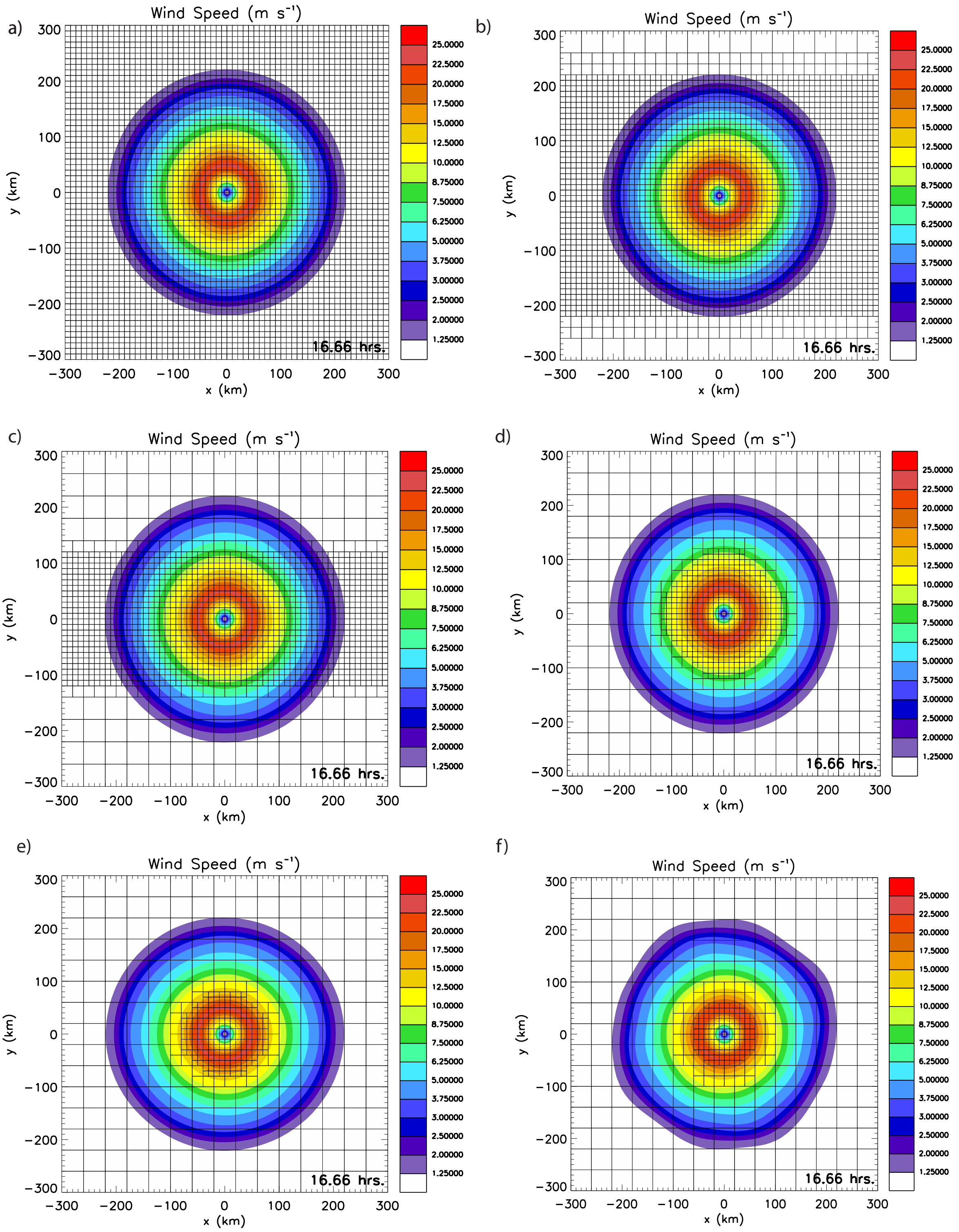

FIG. 5. Simulations of case 1 after a full revolution, at $t = 16.67$ h. Panels: a) FINE, b) SMR2, c) SMR1, d) AMR3, e) AMR2, f) AMR1.

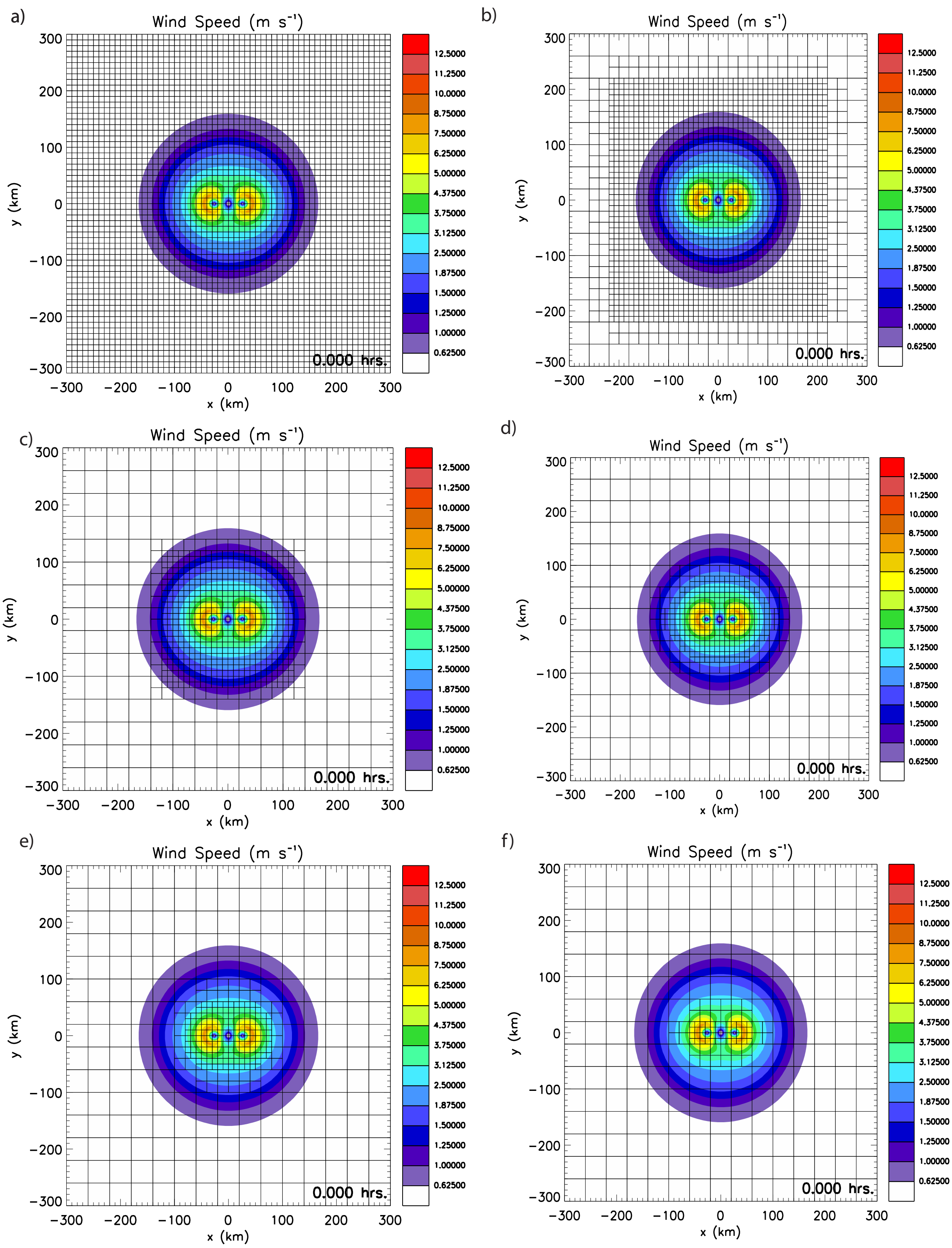

FIG. 6. Initial condition for case 2: Binary vortex interaction. Panels: a) FINE, b) SMR2, c) SMR1, d) AMR3, e) AMR2, f) AMR1.

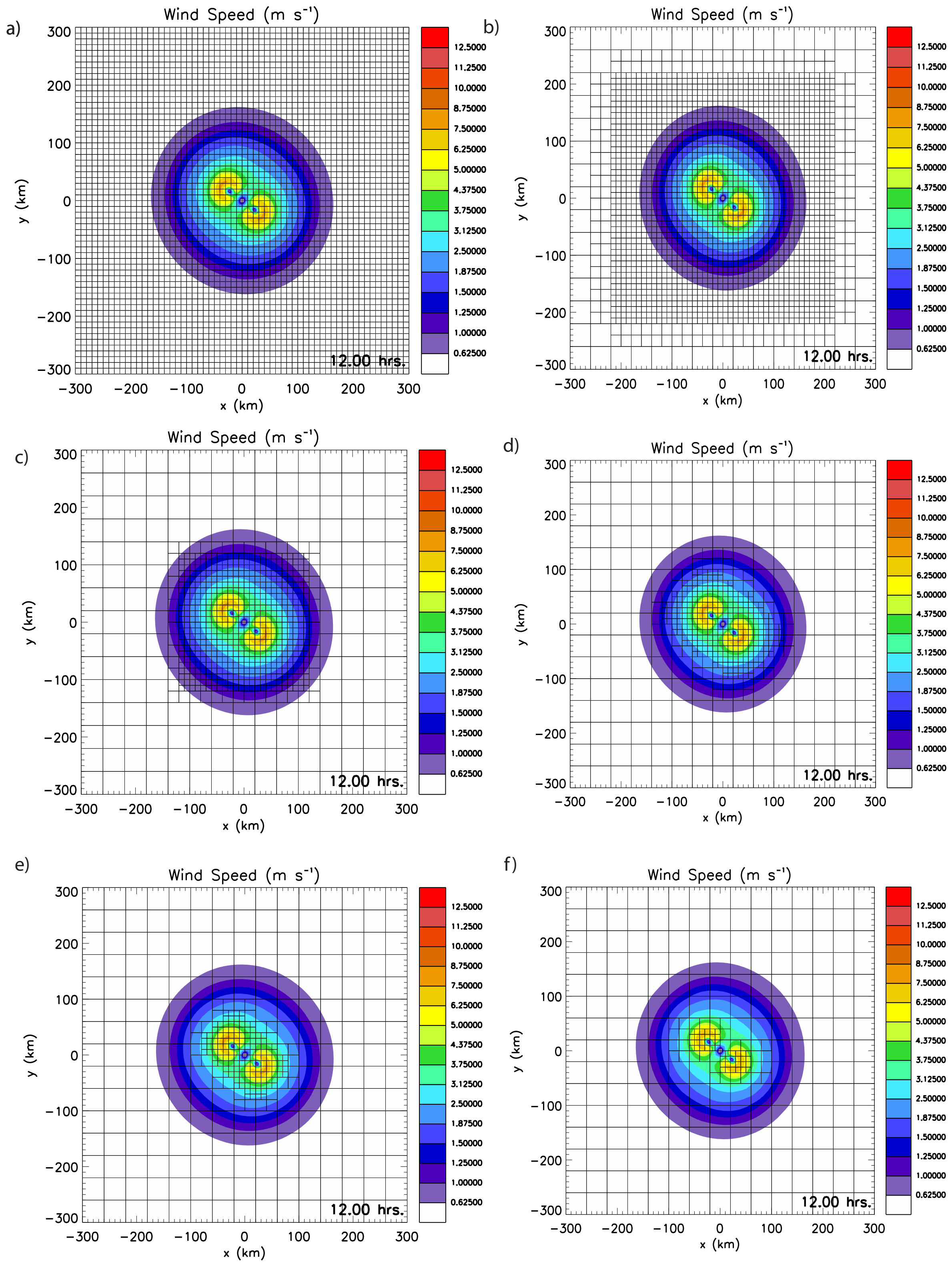

FIG. 7. Simulations of case 2 at $t = 12$ h. Panels: a) FINE, b) SMR2, c) SMR1, d) AMR3, e) AMR2, f) AMR1.

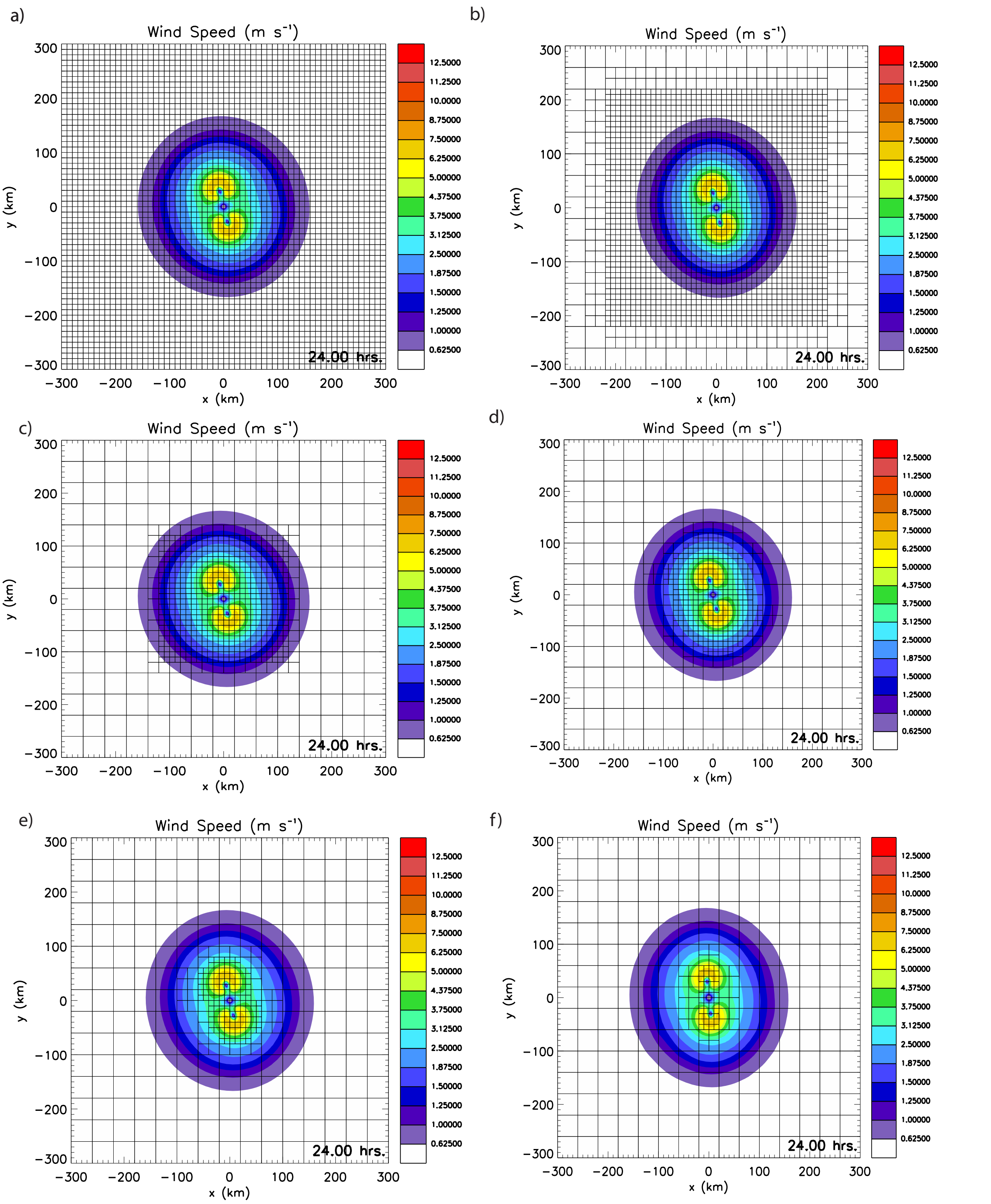

FIG. 8. Simulations of case 2 at $t = 24$ h. Panels: a) FINE, b) SMR2, c) SMR1, d) AMR3, e) AMR2, f) AMR1.

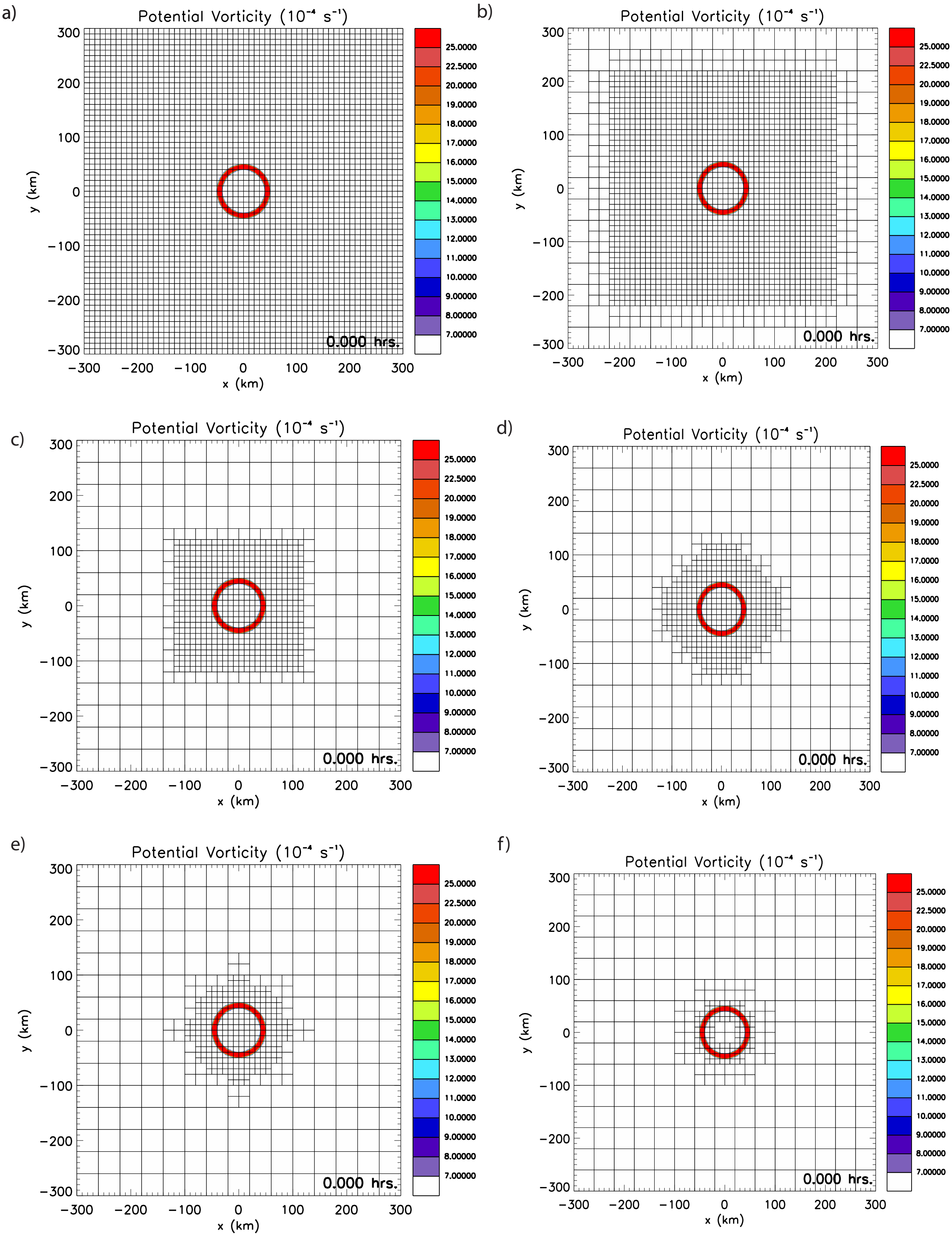

FIG. 9. Initial condition for case 3: unstable vortex. Panels: a) FINE, b) SMR2, c) SMR1, d) AMR3, e) AMR2, f) AMR1.

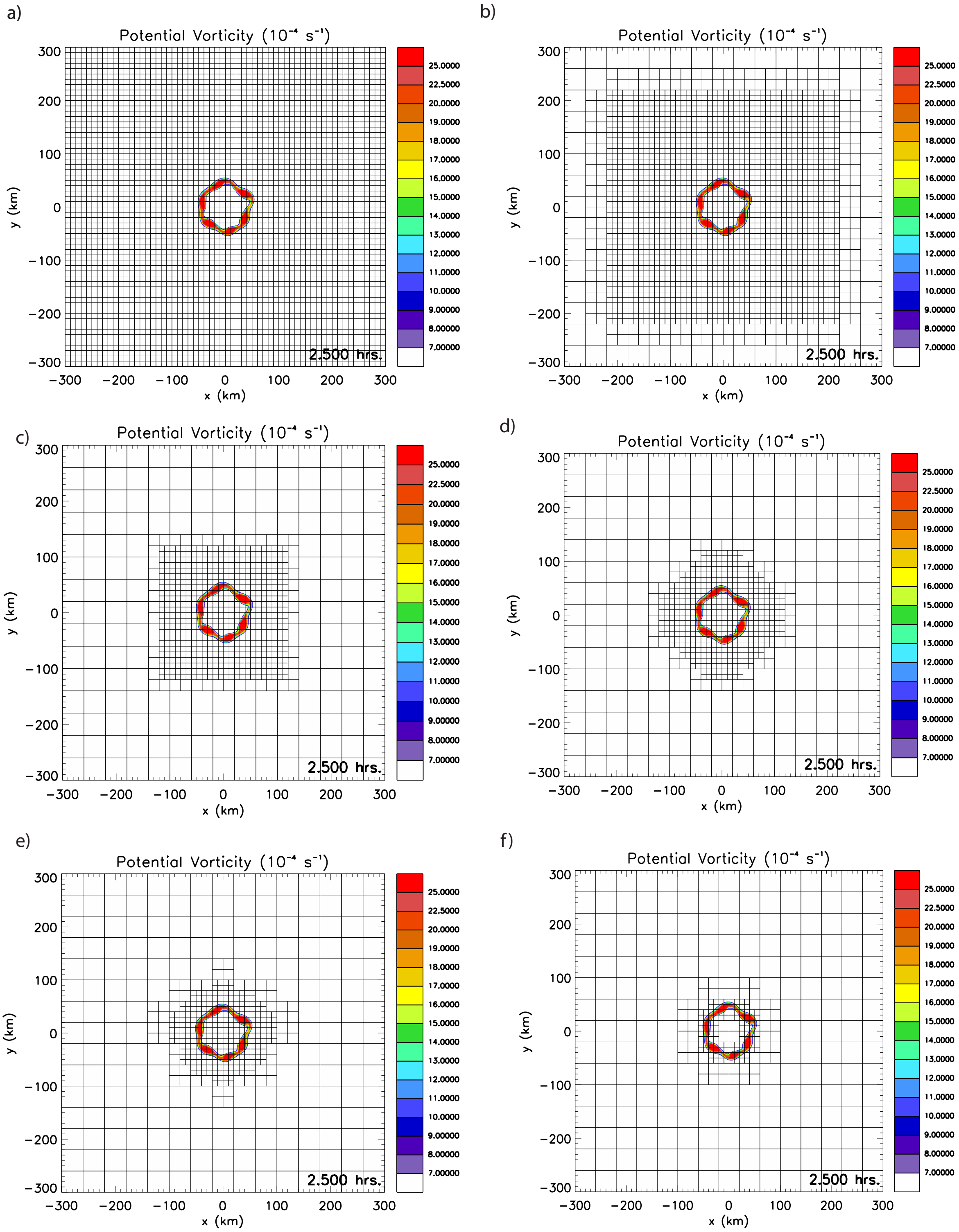

FIG. 10. Simulations of case 3 at t = 2.5 h as barotropic instability occurs. Panels: a) FINE, b) SMR2, c) SMR1, d) AMR3, e) AMR2, f) AMR1.

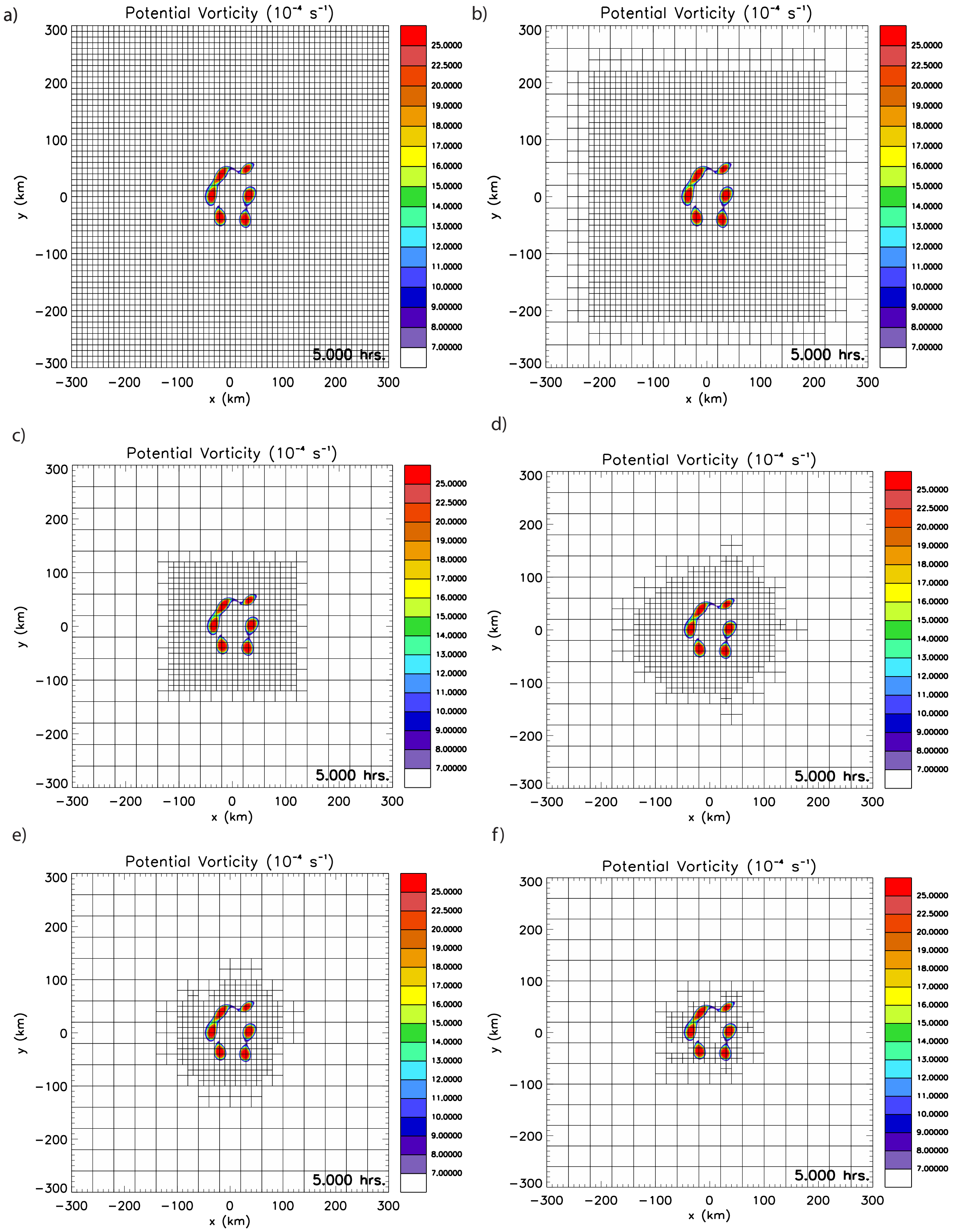

FIG. 11. Simulations of case 3 at $t = 5$ h as mesovortices form. Panels: a) FINE, b) SMR2, c) SMR1, d) AMR3, e) AMR2, f) AMR1.

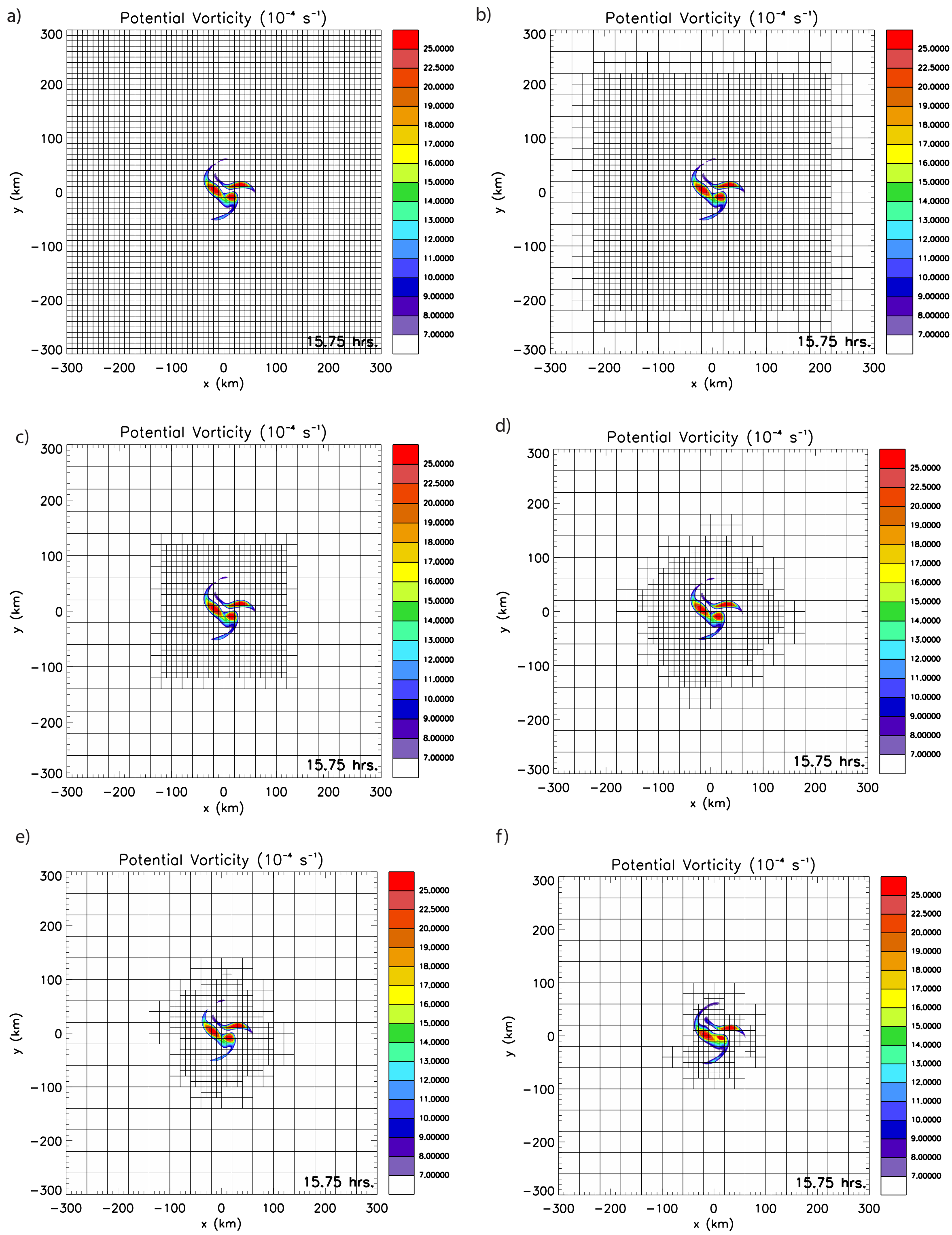

FIG. 12. Simulations of case 3 at t = 15.75 h as the mesovortices merge into a monopole. Panels: a) FINE, b) SMR2, c) SMR1, d) AMR3, e) AMR2, f) AMR1.

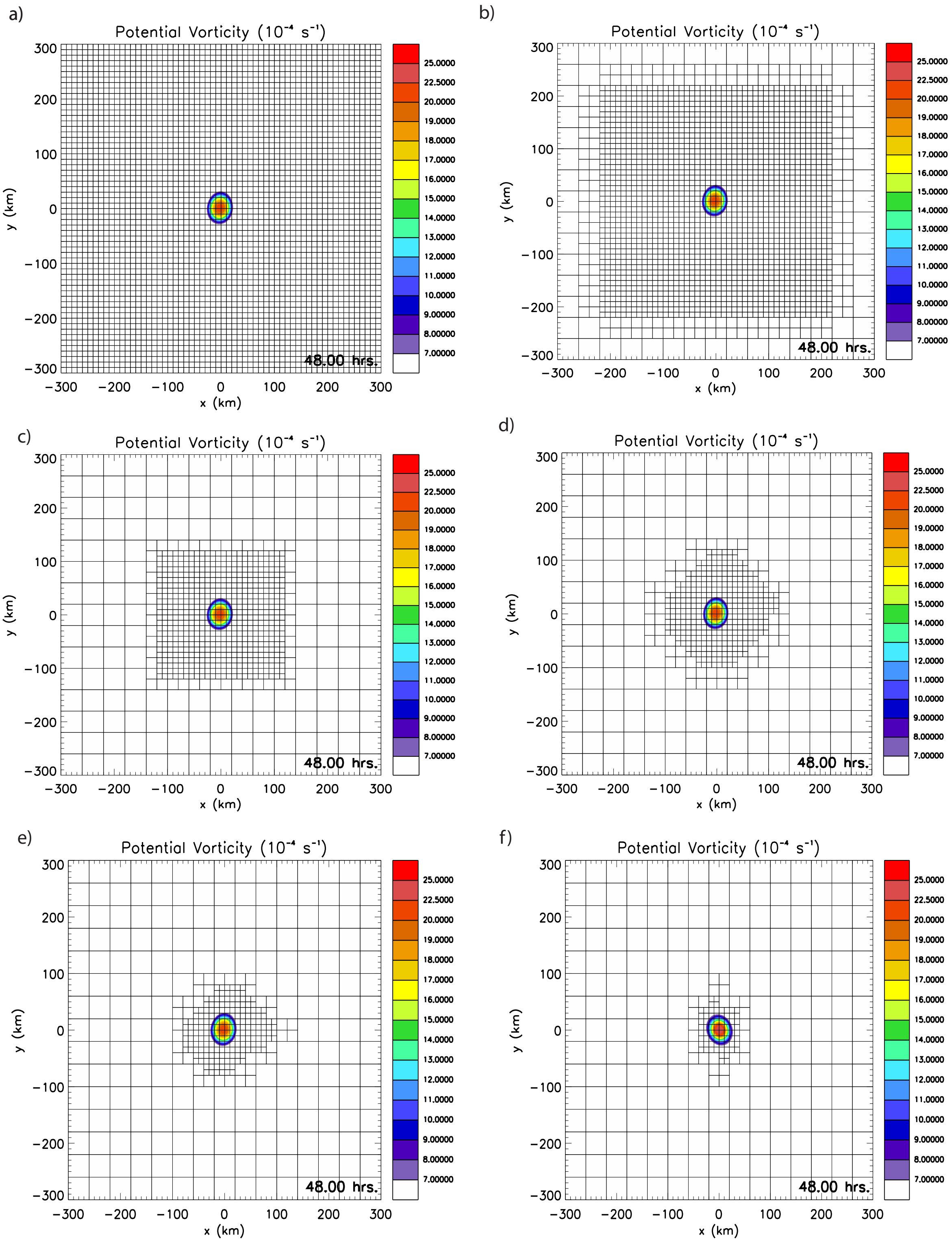

FIG. 13. Simulations of case 3 at $t = 48$ h as the PV ring has broken down and mixed to a monopole. Panels: a) FINE, b) SMR2, c) SMR1, d) AMR3, e) AMR2, f) AMR1.

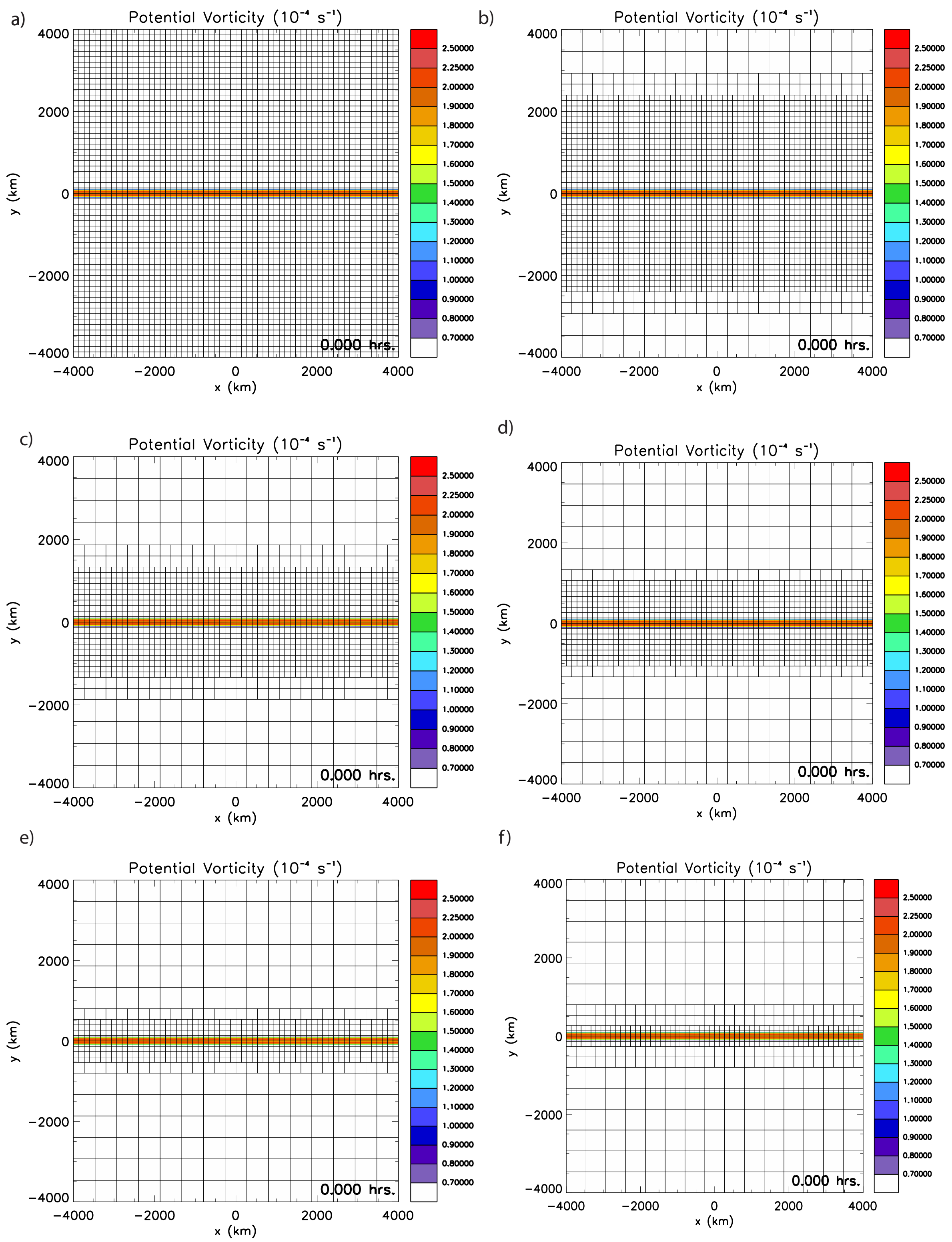

FIG. 14. Initial condition for case 4: strip of PV representing the ITCZ. Panels: a) FINE, b) SMR2, c) SMR1, d) AMR3, e) AMR2, f) AMR1.

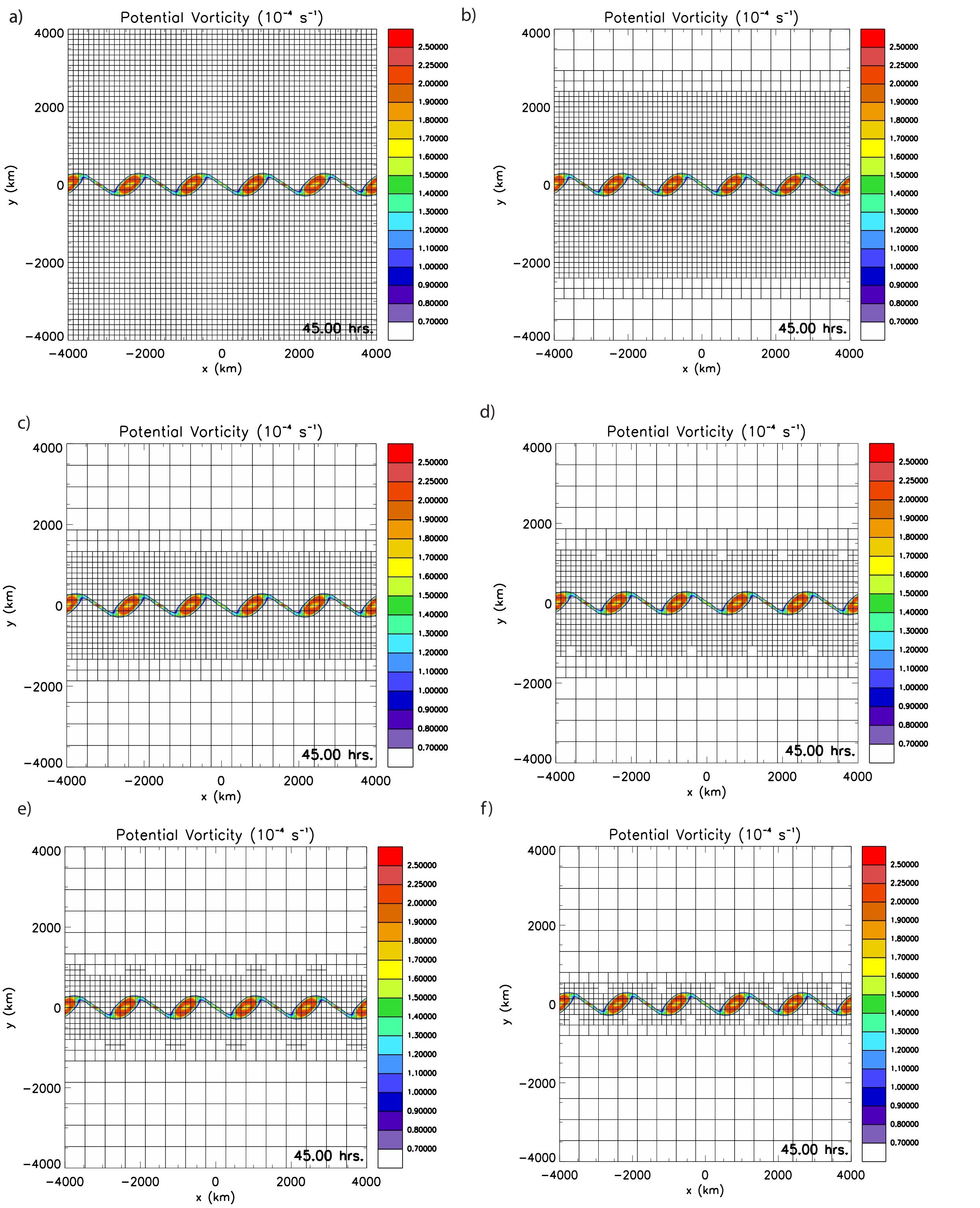

FIG. 15. Simulations of case 4 as barotropic instability sets in at $t = 45$ h. Panels: a) FINE, b) SMR2, c) SMR1, d) AMR3, e) AMR2, f) AMR1.

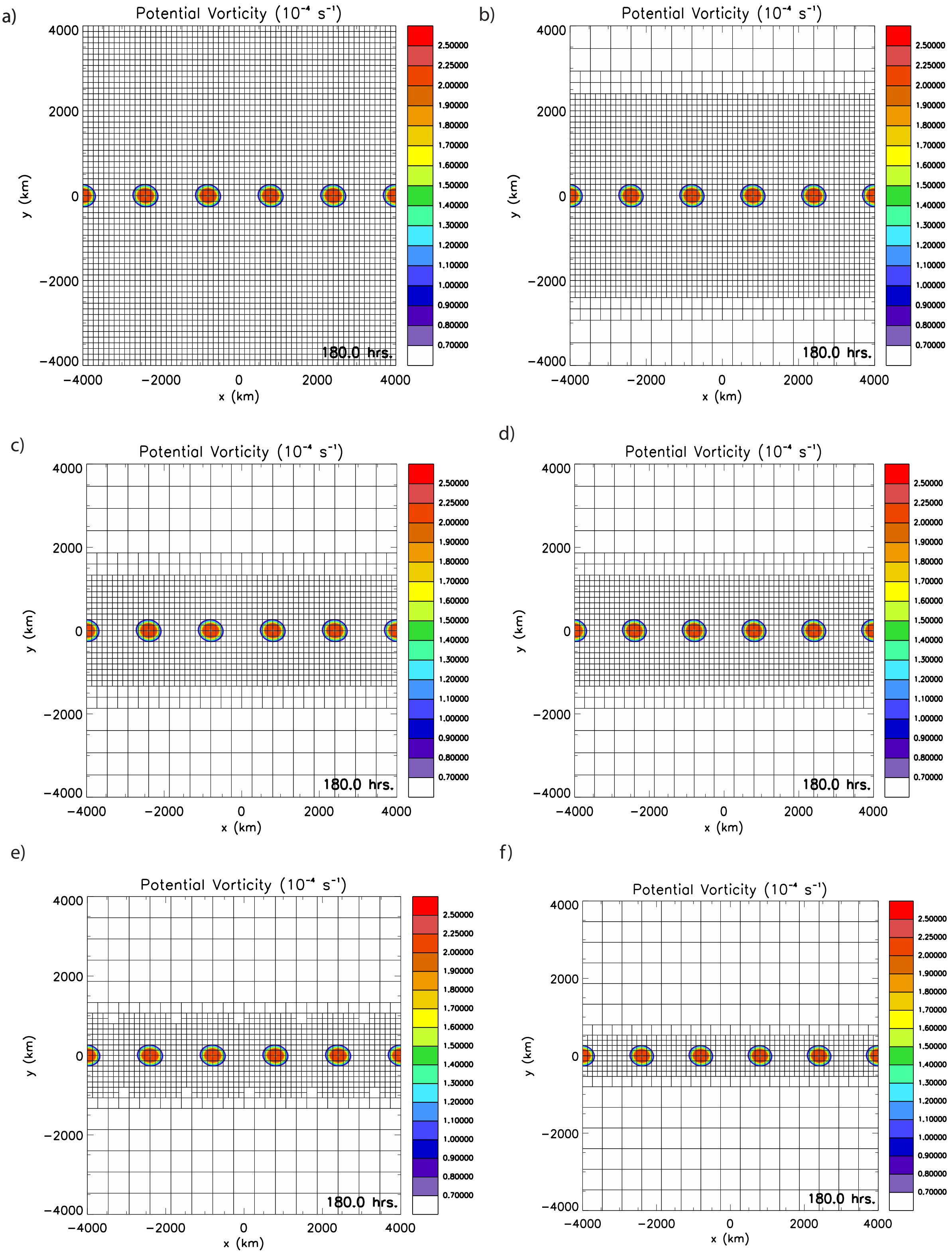

FIG. 16. Simulations of case 4 after multiple TC-like vortices have formed, at t = 180 h. Panels: a) FINE, b) SMR2, c) SMR1, d) AMR3, e) AMR2, f) AMR1.

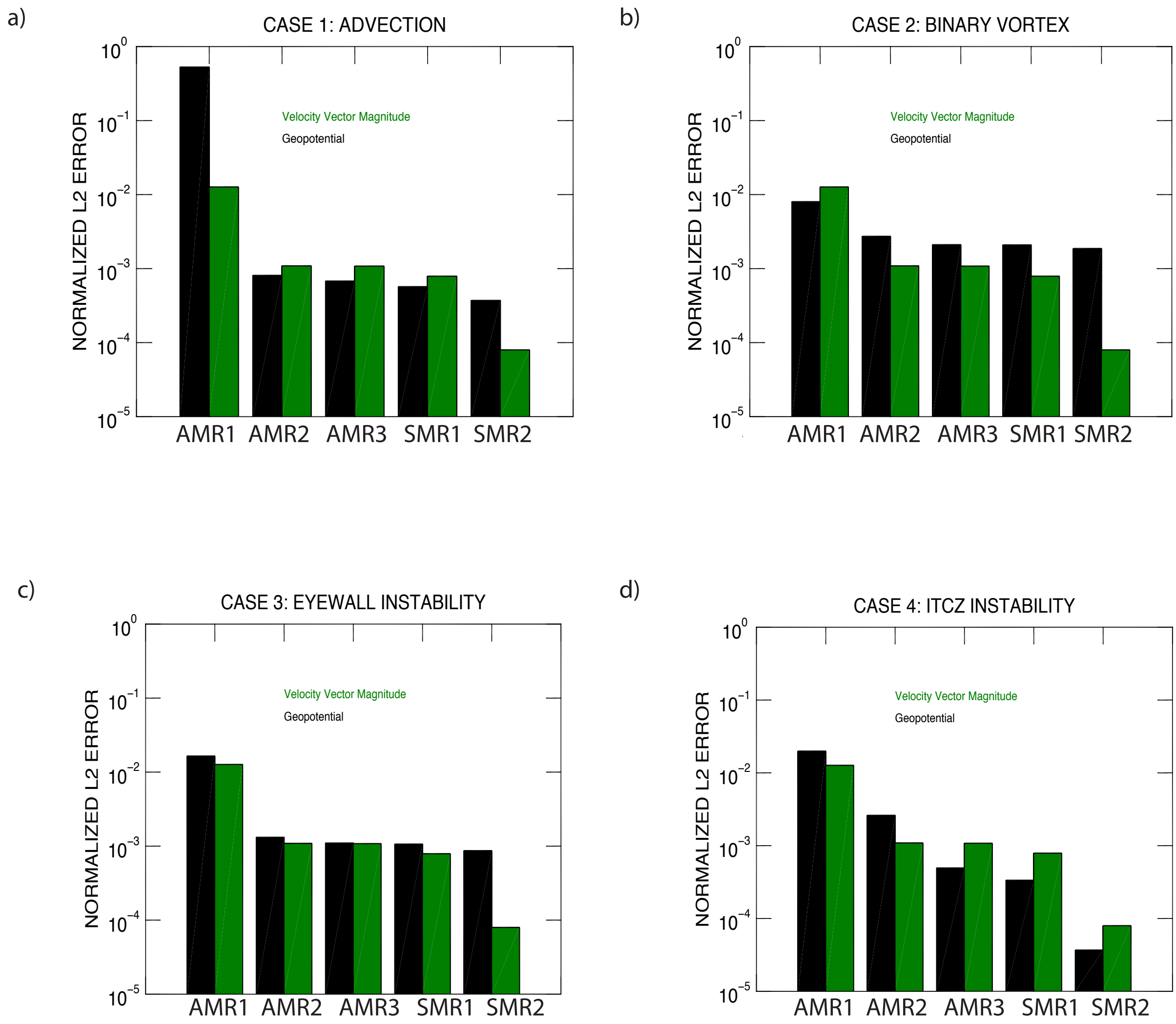

FIG. 17. Normalized L2 Errors for all cases for using all nodal points in the domain. Panels: a) ccase 1: advection, b) case 2: binary vortex, c) case 3: instability, d) case 4: ITCZ. The green bars represent the magnitude of the velocity vector and the black bars represent the geopotential.

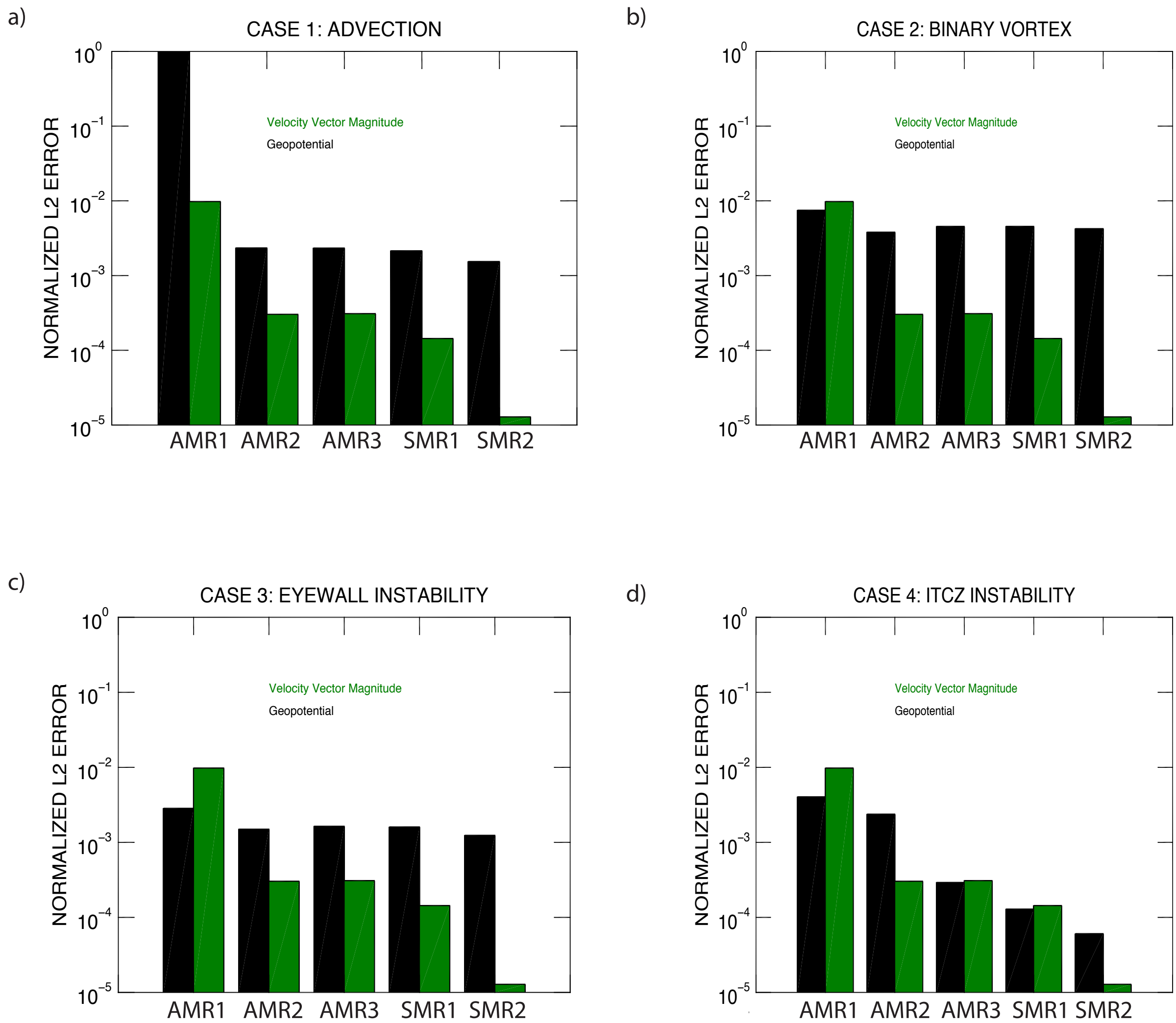

FIG. 18. Normalized L2 Errors for all cases using only nodal points in the localized region of high PV ($r < 100$ km for cases 1–3, $|y| < 500$ km for case 4. Panels: a) case 1: advection, b) case 2: binary vortex, c) case 3: instability, d) case 4: ITCZ. The green bars represent the magnitude of the velocity vector and the black bars represent the geopotential.

a)

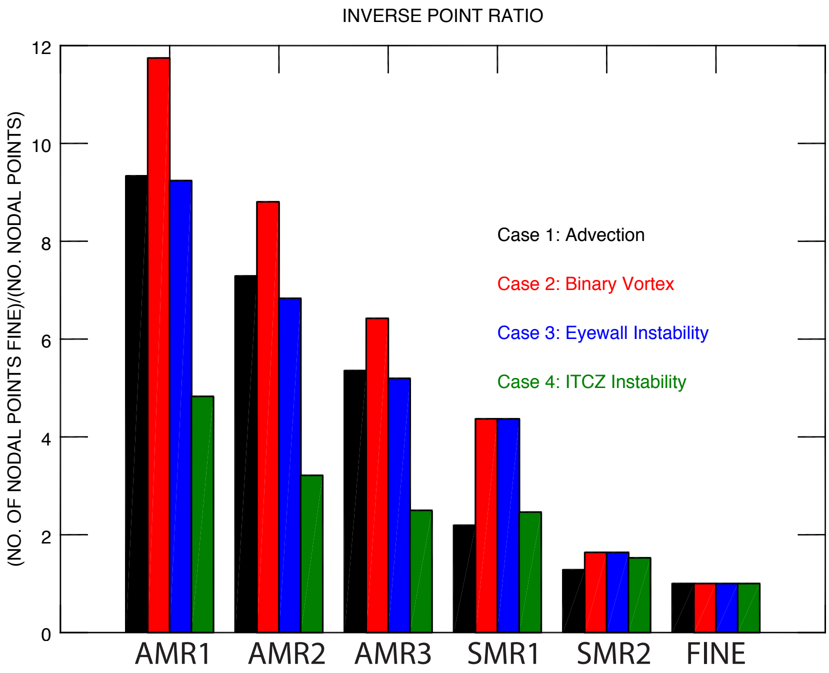

b)

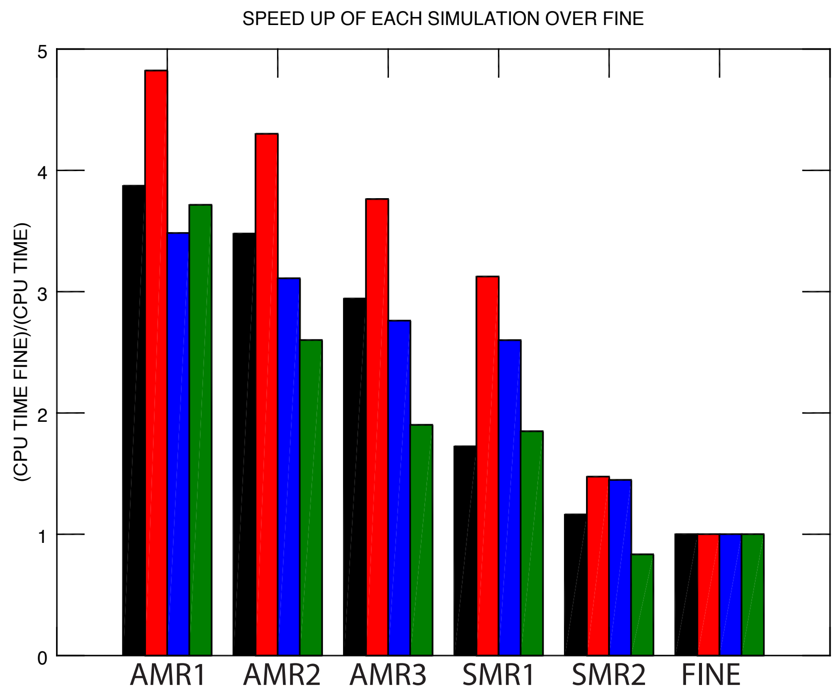

FIG. 19. Panels: a) Ratio of the number of FINE nodal points to the average number of nodal points in each of the other simulations, and b) Ratio of the CPU time of the FINE simulation to the CPU time of each of the other simulations.

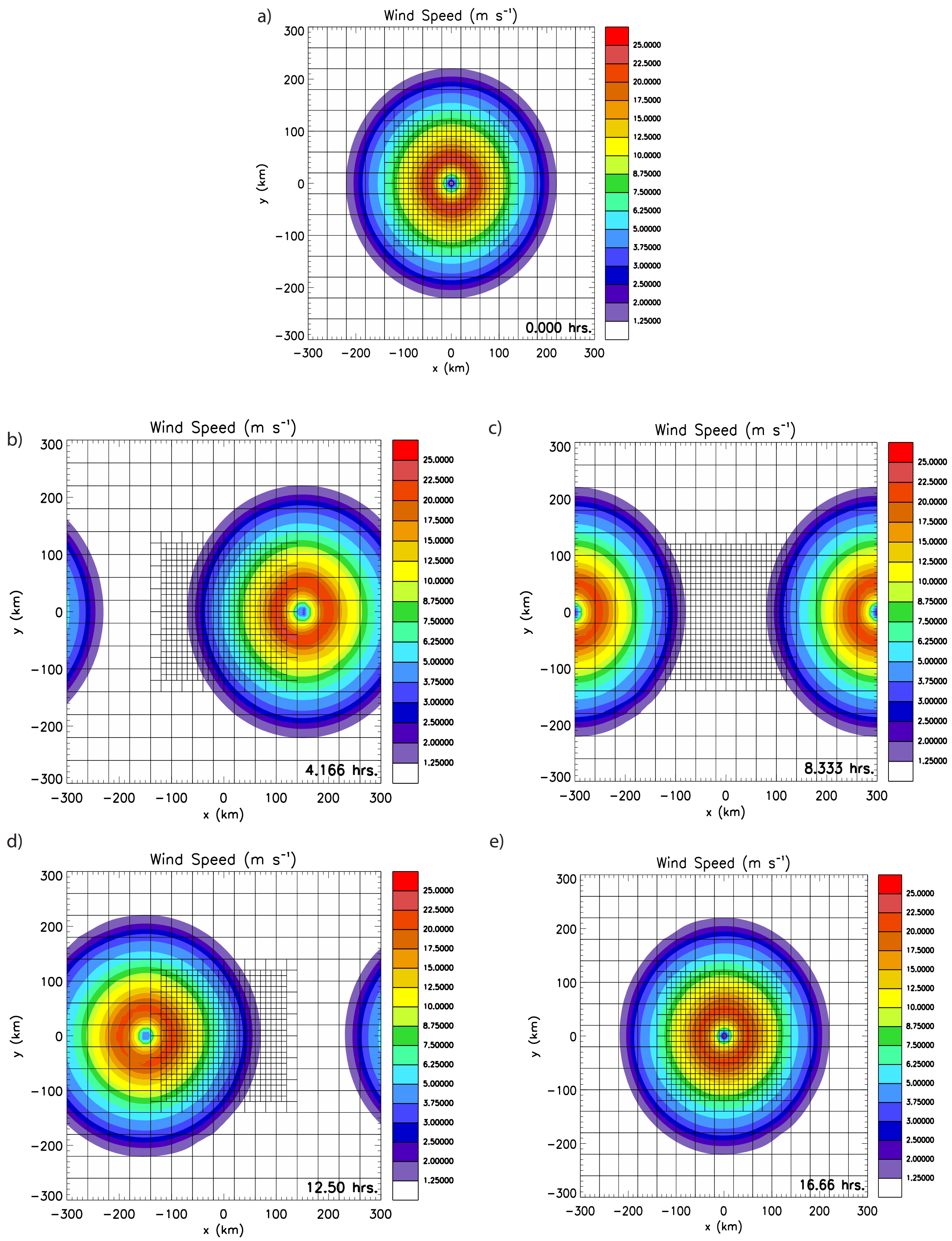

FIG. 20. TC vortex moving through a fixed variable mesh. Panels: a) $t = 0$ h, b) $t = 4.165$ h, c) $t = 8.333$ h, d) $t = 12.5$ h, e) $t = 16.667$ h.